Two-Dimensional Electronic Correlation and Relaxation Spectra: Theory and Model Calculations

Sarah M. Gallagher Faeder[†] and David M. Jonas*

Department of Chemistry and Biochemistry, University of Colorado, Boulder, Colorado 80309-0215

Received: July 26, 1999; In Final Form: October 1, 1999

Hybl et al. demonstrated a technique for recording two-dimensional Fourier transform electronic correlation and relaxation spectra based on detecting phase modulation of the signal electric field in a noncollinear femtosecond four-wave mixing experiment. A theoretical analysis of 2D correlation and relaxation experiments is presented for a system consisting of two electronic states each having two or more sublevels. The separation between absorption and dispersion mode 2D spectra in these experiments is investigated in detail for nonzero pulse duration and compared to related 2D NMR experiments based on a nonlinear optical definition of coherence order. Phase-twisted peaks, which mix absorption and dispersion line shapes, can occur under some circumstances. A 1D projection of the complex 2D spectrum is shown to equal the transient grating signal field, and the real part of this projection is related to the spectrally resolved pump−probe signal. Calculated 2D spectra for a two-level Bloch model, an underdamped Brownian oscillator, and a few models of polar solvent dynamics based on the correlation function approach to the nonlinear response developed by Mukamel and co-workers are presented. The real parts of the 2D spectra are primarily positive (indicative of ground state bleaching and excited state emission) but contain negative regions arising from excitation of coherent superposition states (e.g. vibrational wavepackets) in both the ground and excited electronic states. Assignment of the 2D spectra displaying wavepacket motion at the vibronic level is discussed, and the manifestations of wavepacket motion and vibrational relaxation in the 2D spectra are explored. As suggested by Hybl et al., an increase in pulse duration is found to affect a 2D spectrum primarily as a spectral filter that limits the range of the spectrum. The Gaussian correlation function characteristic of inertial solvent motion is found to be faithfully reflected in a homogeneous 2D cross width which is nearly independent of pulse duration. An alternative experimental method for obtaining only the real part of 2D spectra is proposed.

I. Introduction

Recently, there has been much interest in extending the two-dimensional Fourier transform methods used in magnetic resonance[2,3] to electronic and vibrational spectroscopy using coherent femtosecond excitation.[1,4−10] Two-dimensional spectra correlate molecular oscillation frequencies during two different time intervals. Fourier transformation of a nonlinear signal with respect to two time intervals produces a spectrum with two frequency axes. A peak in a 2D spectrum indicates that oscillation at ω_1 during the first time interval gave rise to oscillation at ω_2 during the second interval. Two-dimensional spectra help separate and correlate peaks; Fourier transform techniques have the advantage of molecule limited resolution in both time and frequency. 2D FT spectroscopy has proven to be a tremendously powerful method for NMR studies of large molecules and biomolecules.

Recent interest in femtosecond 2D FT methods has arisen partly from attempts to investigate systems where partially overlapping bands and fast dynamics can combine to partly frustrate frequency selective pump−probe experiments (e.g. vibrational energy transfer and relaxation in liquids[11] and proteins,[12] polar solvent reorganization during charge transfer,[13−15] the dynamic local hydrogen-bonding structure of water,[16] electronic coupling and energy transfer in aggregates[17,18]). The problem arises from the Fourier transform limit imposed by the pulses: a short pulse must have a broad spectrum. Following the pioneering experiments of Shank and co-workers,[19−21] several groups have spectrally resolved short probe pulses after they traversed a pumped sample. This allows coherent molecular radiation in the probe direction, which may continue after the probe exits the sample, to set the Fourier transform limit for probe frequency and time resolution. However, the pump pulse still imposes an externally fixed Fourier transform limited trade-off between time resolution and frequency resolution. Longer pump pulses have been useful for selective excitation,[21,22] but it is difficult to distinguish among strongly coupled chromophores, fast relaxation dynamics between bands during a longer pulse, or imperfectly selective excitation caused by intrinsically overlapping bands. 2D FT spectra could provide the pump−probe correlation with molecule-limited resolution in *both* frequency dimensions. 2D correlation spectra should also reveal transient inhomogeneities and distinguish distributions of single chromophore site energies from distributions of couplings between chromophores.

There have been a number of femtosecond experiments as a function of two time variables. Following the practice in NMR, only experiments with two frequency dimensions will be referred to as two-dimensional. Ernst and co-workers suggested that

* Address all correspondence to this author at the Department of Chemistry and Biochemistry, CB 215, University of Colorado at Boulder, Boulder, CO 80309-0215. Tel. (303)492-3818. Fax (303)492-5894. E-mail: David.Jonas@colorado.edu.

[†] Current address: Department of Physics of Complex Systems, Weizmann Institute of Science, 76100 Rehovot, Israel.

10.1021/jp9925738 CCC: $18.00
Published on Web 11/12/1999

extensions of 2D NMR to microwave and infrared spectroscopy might be useful.[23] The number of experimental and theoretical studies of 2D spectra outside magnetic resonance is relatively small. High-frequency resolution two-dimensional microwave[24,25] and rotational Raman[26,27] correlation spectra have been reported. Tanimura and Mukamel proposed fifth-order nonlinear femtosecond 2D Raman vibrational spectroscopy.[4] Lepetit and Joffre demonstrated an absolute value 2D spectrum reflecting bulk phase-matching of sum frequency mixing in a thick potassium dihydrogen phospate (KDP) crystal.[28] Tokmakoff et al. reported 2D FT Raman vibrational spectra,[5] though there is now evidence[29] that the 2D Raman spectra are dominated by cascaded third-order nonlinear Raman signals[30] which do not provide the microscopic information the fifth-order experiments were designed to measure. In contrast to the difference frequencies and absolute value spectra recorded in the 2D femtosecond correlation experiments,[5,28] Hybl et al.[1] recovered separate absorption and dispersion 2D spectra as a function of two electronic frequencies in a noncollinear three-pulse experiment which produced 2D correlation spectra for zero delay between the second and third pulses and 2D relaxation spectra for nonzero delay. Hybl et al. also outlined a theoretical treatment of 2D spectra in the optical Bloch limit and demonstrated a 2D Raman-electronic correlation spectrum.[1] The treatment presented here is limited to 2D electronic spectra generated by Fourier transformation of two time delays. Hochstrasser and co-workers have used spectrally resolved pump−probe experiments with a narrowband tunable pump and a broadband probe to construct 2D infrared spectra which contain both positive and negative regions.[12] Recent theoretical work has treated two-dimensional infrared,[8] terahertz,[6] and electronic[10] correlation spectra in absolute value mode.

The power of 2D FT techniques over conventional techniques such as pump−probe comes from the exploitation of coherence and phase information. As in 1D FT spectroscopy, the frequency resolution of 2D FT spectra is limited only by the maximum separation between pulses used to generate the measured signal, not by the pulse bandwidth. This completely solves the problem of trading off time resolution for frequency resolution and opens the door to a universal femtosecond spectrometer. Since 2D spectra reveal correlations between transitions, 2D spectra have approximately homogeneous line widths in each frequency dimension.

Pump−probe techniques also suffer from an exceedingly difficult to interpret feature, commonly referred to as the coherence spike, when the pulses overlap. This makes it impossible to excite selectively one band in a crowded spectrum and follow the undistorted dynamics which give rise to the line width of the band: they all occur during the pulse overlap. A similar problem also plagues standard femtosecond photon echo techniques, where the early time behavior of the correlation function is obscured[31,32] by the rapid third-order free induction decay of an inhomogeneous ensemble.

Absolute value 2D spectra combine both real absorption line shapes and imaginary dispersion line shapes. Because dispersion line shapes are broad, decaying as $1/(\omega - \omega_0)$, absolute value spectra are not nearly so useful as separate absorption and dispersion spectra for the spectrally congested systems on which 2D FT spectra realize their full power. Even if a 2D spectrum is purely absorptive or dispersive, absolute value spectra do not reveal the signs of the peaks and thus cannot distinguish excited state absorption from emission or reveal some of the subtler signed features in 2D spectra to be discussed here. The design of the 2D experiment can affect the shape of peaks in absolute value power spectra. In order to separate the real (absorptive) and imaginary (dispersive) contributions to 2D FT spectra, it is absolutely necessary to measure the signal field at the sample.

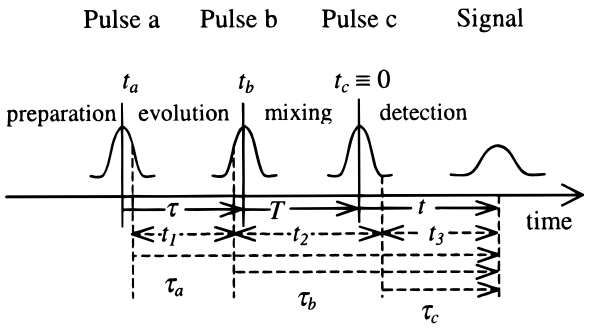

Figure 1. Timing diagram. Pulses a, b, and c are distinguished by their wave vectors. The experimentally controlled times at which the center of each pulse arrives at the sample are t_a, t_b, and t_c. The zero of time t is chosen to coincide with the center of pulse c ($t_c \equiv 0$) so that t_a and t_b are negative. As in 2D NMR, the time intervals between pulses are labeled preparation (up to and including the first pulse), evolution $\tau \equiv t_b - t_a$ (between the first and second pulses), mixing $T \equiv \min(|t_a|, |t_b|)$ (which includes the second and third pulses), and detection t (after the third pulse). 2D electronic spectra are generated by Fourier transformation of the signal field with respect to t (detection) and τ (evolution). The positive time intervals t_1, t_2, and t_3 between perturbation theoretic field−matter interactions (which can occur at any time during a pulse) appear in the double-sided Feynman diagrams representing terms in density matrix perturbation theory and are always numbered consecutively regardless of which pulse interacts first. The intervals τ_a, τ_b, and τ_c are pulse-labeled interaction intervals used in calculating the nonlinear polarization from the response function.

To generate 2D spectra, Hybl et al.[1] used the method introduced by Gallagher et al.[33] to measure the electric field of a fully noncollinear three-pulse scattering signal at the sample. In a three-pulse scattering experiment,[34,35] pulses with wave vectors $\boldsymbol{k_a}$, $\boldsymbol{k_b}$, and $\boldsymbol{k_c}$ cross in the sample and the signal radiated into a fourth phase-matched direction with wave vector $\boldsymbol{k_c} + \boldsymbol{k_b} - \boldsymbol{k_a}$ is detected. A macroscopically phased array of molecular dipoles is required for radiation of a coherent pulse of light in a given direction. The excitation pulse direction and timing can be chosen to selectively detect the set of density matrix coherence pathways between molecular states that yield the required spatially dependent dipole phase.[36] The pulse timing is illustrated in Figure 1. The first pulse excites electronic dipoles which oscillate until the arrival of the second pulse. Depending on the timing of the second pulse, the dipole oscillation frequency, and the spatial position, these oscillations can be amplified (increasing the excited state population and depopulating the ground state) or suppressed (transferring all population back to the ground state) by the second pulse. The first pulse can be either a or b, so the delay $\tau \equiv t_b - t_a$ can be either positive or negative. The first two pulses excite a spatially periodic electronic state population grating in the sample. This population grating produces both absorption coefficient and refractive index gratings.[37] The grating wavelength depends on the electronic frequency and the crossing angle between pulses a and b. The grating phase (positions of maximum excited state population within the grating) depends on the electronic frequency and the pulse delay. The time T between the second pulse (a or b) and the third pulse (c) allows vibrational wavepacket motion and relaxation. After pulse c hits the grating, the field radiated into the signal direction is detected as a function of time t. If it is remembered that reradiation from vibrating molecules can generate frequency shifts, this phase-matched radiation can be viewed as diffraction of pulse c off the grating excited by a and b.

For $T = 0$, the pulse sequence matches 2D NMR correlation spectroscopy (COSY),[3] which is used to probe spin−spin coupling. For $T > 0$ the pulse sequence matches 2D NMR nuclear Overhauser effect spectroscopy (NOESY),[3] which is a relaxation spectroscopy used to probe dipole−dipole spin excitation transfer. Standard 2D NMR labels[2] for the time intervals are given in Figure 1. The acronym EASY 2D has been proposed for this optical experiment, which is based on a five-beam interferometer. EASY stands for echo argument spectroscopy since the key to the experiment is recovery of electronic frequencies by detecting phase (argument) modulation of the echo signal field at the initial excitation frequency.[1,33,38] Since this phase modulation is stored in a spatial population grating, it can be detected even after the original electronic coherence has completely decayed, making it possible to see phenomena that take place over relatively long times. 2D electronic spectra are generated by measuring the electric field of a three-pulse scattering signal and Fourier transforming with respect to the detection time after the third pulse, t (yielding frequency axis ω_t) and the dipole evolution time between the first and second pulses, τ (yielding frequency axis ω_τ).

To avoid mixing absorption and dispersion mode 2D spectra, it is necessary to superpose equally weighted signals with equal and opposite "orders of coherence" during the dipole evolution period.[2] The Fourier transform procedure must also be chosen to match the experiment in order to avoid inadvertent Kramers−Kronig transformation between absorption and dispersion mode spectra.[38] Hybl et al.[1] combined a standard three-pulse echo procedure[35] for scanning continuously across $\tau = 0$ at constant T with complex Fourier transformation over the range $-\infty < \tau < \infty$ to do this. A nonlinear optical definition for order of coherence is proposed here in order to examine this procedure in more detail.

A simple and useful (but incomplete) interpretation which has suggested a number of correct results views the real part of the complex 2D spectrum as showing the effect of initial absorption at frequency ω_τ on subsequent absorption and emission at frequency ω_t. A positive peak in the real part of the spectrum indicates that excitation at ω_τ increases the subsequent transmission through the sample at ω_t (this usage differs in sign from typical usage in NMR). For example, if the 2D spectrum consisted of a positive ridge along the diagonal line $\omega_t = -\omega_\tau$, excitation at ω_τ resulted in a transmission increase only at $\omega_t = -\omega_\tau$, indicating the sample consists of an inhomogeneously broadened ensemble of two-level systems. The incompleteness of this view arises when coherent excitation of strongly coupled multilevel systems is considered: it cannot be stated which frequency is absorbed in excitation of a coherent superposition state. A precisely correct statement is that EASY 2D spectra reveal the effect of each initial dipole oscillation frequency on the amplitude and phase of every final dipole oscillation frequency. In some cases, the connection between real/imaginary and absorption/dispersion is not yet clear. The 2D spectra are then labeled only real or imaginary and no assignment to absorptive or dispersive parts of the third order susceptibility is implied. A closely related 2D experiment (acronym HARD 2D) is proposed to selectively detect only the real part of the EASY 2D spectrum.

II. Theory

With the exception of a recent treatment of 2D terahertz spectroscopy by Okumura and Tanimura,[6] theoretical treatments of 2D spectroscopy[10] have assumed that delayed pulses have the "carrier wave" form used in magnetic resonance.[39] Carrier wave delayed pulses are produced by multiplying a single continuous (carrier) wave by a variably delayed envelope. Optical carrier wave delayed pulses can be generated by pulse shaping techniques.[40,41] In the experiments reported by Hybl et al.,[1] pulse delays were generated by moving a mirror in one arm of an interferometer. Albrecht et al. have discussed how the method of pulse delay generation is critical for phase-resolved nonlinear optics and recovery of electronic frequencies in 2D spectroscopy.[38] The linearly polarized pulses here are taken to have the "envelope delayed form" generated by an interferometer pathlength difference

$$E_\alpha(t) = e(t - t_\alpha)\cos[\phi(t - t_\alpha)] \tag{1}$$

where $e(t)$ is the temporal envelope (e.g. a Gaussian $e(t) = e_0 \exp(-2\ln[2]t^2/t_p^2)$ with intensity full width at half-maximum t_p), $\phi(t)$ is the temporal phase (e.g. $\phi(t) = \omega_0 t$), and $t_\alpha = \Delta l_\alpha/c$ is the delay generated by the path difference Δl_α. The third-order nonlinear polarization with wave-vector $\boldsymbol{k_s}$ can be obtained by a triple convolution of the phase-matched part of the impulse response function with the incident electric fields.

$$P^{(3)}(\boldsymbol{k_s},t,t_a,t_b) = \int_0^\infty \int_0^\infty \int_0^\infty S^{(3)}(\boldsymbol{k_s},\tau_a,\tau_b,\tau_c)E_a(t-\tau_a)\times E_b(t-\tau_b)E_c(t-\tau_c)\,d\tau_a\,d\tau_b\,d\tau_c \tag{2}$$

The center of pulse c defines $t = 0$. The phase-matched part of the third-order response function $S^{(3)}(\boldsymbol{k_s},\tau_a,\tau_b,\tau_c)$ is equal to the polarization with wave vector $\boldsymbol{k_s} = \sum s_\alpha \boldsymbol{k}_\alpha$ (where $s_\alpha = \pm 1$ and α = a, b, c) created by three delta function excitation pulses with wave vectors $\boldsymbol{k_a}$, $\boldsymbol{k_b}$, and $\boldsymbol{k_c}$ at the times τ_a, τ_b, and τ_c before the present. Since the time domain electric fields and nonlinear polarization are real-valued functions, $S^{(3)}(\boldsymbol{k_s},\tau_a,\tau_b,\tau_c)$ is real. By causality, $S^{(3)} = 0$ if any $\tau_\alpha < 0$. The vector nature of the fields and tensorial character of $S^{(3)}$ are ignored.[42] The frequency domain fields and polarization are defined by the inverse Fourier transform

$$\hat{E}(\omega_t) = \int_{-\infty}^{\infty} E(t)\exp(i\omega_t t)\,dt \tag{3}$$

and are inherently complex-valued functions over the entire real axis $-\infty < \omega_t < \infty$. Since two frequencies are used, frequencies are given a subscript denoting the conjugate Fourier transform time variable. Because $E(t)$ is real

$$\hat{E}(\omega_t)^* = \hat{E}(-\omega_t) \tag{4}$$

Phase shifts are defined as constant spectral phase shifts in the frequency domain, which multiply $\hat{E}_\alpha(\omega_\alpha)$ by $\exp[i\phi_\alpha\,\mathrm{sign}(\omega)]$.[38] A triple inverse Fourier transformation of eq 2 with respect to t_a $(-\omega_a)$, t_b (ω_b), and t $(\omega_t = \omega_c + \omega_b - \omega_a)$ yields the complex polarization in the frequency domain.[38] The frequency variables used in the transformations with respect to t_a, t_b, and t are chosen so the sign of the excitation frequency ω_α in the signal frequency $\omega_s = \sum s_\alpha \omega_\alpha$ matches the sign of the corresponding wave vector.

$$\hat{P}^{(3)}(\boldsymbol{k_s},(\omega_c + \omega_b - \omega_a),-\omega_a,\omega_b) = \hat{S}^{(3)}(\boldsymbol{k_s},-\omega_a,\omega_b,\omega_c)\hat{E}_a(-\omega_a)\hat{E}_b(\omega_b)\hat{E}_c(\omega_c) \tag{5}$$

$\hat{S}^{(3)}$ is the inverse Fourier transform of the third-order response function $S^{(3)}$ with respect to τ_a, τ_b, and τ_c. $\hat{E}_\alpha(\omega_\alpha)$ is the inverse Fourier transform of $E_\alpha(t)$ at zero delay ($t_\alpha = 0$). The frequency variables used for t_a, t_b, and t dictate the conjugate Fourier transform frequencies for $\tau_a(-\omega_a)$, $\tau_b(\omega_b)$, and $\tau_c(\omega_c)$ in this transform. According to eq 5, constant spectral phase shifts ϕ_α

of the excitation pulses produce a constant spectral phase shift $\phi_s = \sum s_\alpha \phi_\alpha$ of the source polarization.[38,43] The three-dimensional result in eq 5 also suggests that the effect of finite duration pulses on a 2D spectrum is simply one of spectral filtering (and possibly phase distortion via chirp).[1] Numerical investigations of this suggestion are presented in this paper. Since $S^{(3)}(\boldsymbol{k}_s,\tau_a,\tau_b,\tau_c)$ is real, the real and imaginary parts of the frequency domain third-order phase-matched susceptibility obey[44]

$$\hat{S}^{(3)}(\boldsymbol{k}_s,-\omega_a,\omega_b,\omega_c)^* = \hat{S}^{(3)}(\boldsymbol{k}_s,\omega_a,-\omega_b,-\omega_c) \qquad (6)$$

The real (dispersive or reactive) part of the frequency domain phase-matched nonlinear susceptibility yields no net change in material energy, while the imaginary (absorptive or dissipative) part mediates energy exchange between material and the electromagnetic field.[43,44]

In calculations which invoke the rotating wave approximation, it is convenient to use complex electric fields, a complex third-order response function, and a complex third-order polarization.[36] The complex field associated with the real field in eq 1 is defined by

$$\hat{E}(t) = (1/2)\hat{e}(t - t_\alpha)\exp[i\omega_0(t - t_\alpha)] \qquad (7)$$

so that $E(t) = \hat{E}(t) + \hat{E}^*(t)$. The complex envelope $\hat{e}(t - t_\alpha) = e(t - t_\alpha)\exp[i(\phi(t - t_\alpha) - \omega_0(t - t_\alpha))]$ is a useful way to incorporate chirp and phase shifts. The complex field is independent of the reference frequency ω_0. Within the rotating wave approximation, the third-order polarization is given by

$$\begin{aligned} P^{(3)}(\boldsymbol{k}_{sa},t,t_a,t_b) = \int_0^\infty \int_0^\infty \int_0^\infty \hat{S}^{(3)}_{rw}(\boldsymbol{k}_{sa},\tau_a,\tau_b,\tau_c) \times \\ \hat{e}_a^*(t - t_a - \tau_a)\hat{e}_b(t - t_b - \tau_b)\hat{e}_c(t - \tau_c) \times \\ \exp[i\omega_a(t - t_a - \tau_a)]\exp[-i\omega_b(t - t_b - \tau_b)] \times \\ \exp[-i\omega_c(t - \tau_c)]\, d\tau_a\, d\tau_b\, d\tau_c + \text{complex conjugate} \end{aligned} \qquad (8)$$

where $\hat{S}^{(3)}_{rw}$ is the rotating wave approximation to the phase-matched response function. t_a and t_b are the experimentally controlled pulse delays relative to the center of pulse c at $t = 0$. Writing the response function in terms of the pulse-labeled interaction times τ_a, τ_b, and τ_c instead of the ordered times t_1, t_2, and t_3 simplifies the form of eq 8.[43]

The third-order response function $\hat{S}^{(3)}_{rw}(\boldsymbol{k}_{sa},\tau_a,\tau_b,\tau_c)$ can be calculated by third-order perturbation theory. Density matrix perturbation theory is convenient because each term in the perturbation series has a definite wave vector, so that only terms which contribute to a macroscopically near phase matched polarization for the detected signal direction need be retained.[36,45] For a two-electronic-state system, each surviving term in the perturbation series for emission in direction $\boldsymbol{k}_c + \boldsymbol{k}_b - \boldsymbol{k}_a$ is represented by one of the eight double-sided Feynman diagrams D_1-D_8 shown in Figure 2 (or by a conjugate diagram terminating in the matrix element ρ_{ge} instead of ρ_{eg} which makes a complex conjugate contribution to the signal). Rules for correspondence between terms in the perturbation series[46] and diagrams can be found in the books by Shen[45] and Mukamel.[36]

Figure 2 shows double-sided Feynman diagrams representing terms in the density matrix perturbation theory expansion of the nonlinear response for a two-electronic-state system in which excited state sublevels are labeled e or e′ and ground state sublevels are labeled g or g′. The excitation pulse interactions are represented by arrows intersecting the vertical lines on each side of the diagram. The density matrix element change probed between interactions is indicated by the labels mn, (m,n = g, g′, e, e′) where mn represents the density matrix element ρ_{mn}. For finite duration pulses, the positive time intervals t_1, t_2, and t_3 can range around $t_1 = |\tau|$, $t_2 = T$, and $t_3 = t$, as indicated by the triple convolution in eq 8. Diagrams D_5-D_8 have an improper time ordering and do not contribute to the signal unless pulse c overlaps a or b. During the evolution time τ, the electronic dipoles are oscillating at frequencies (such as ω_{ge} in diagram D_2) which appear on the ω_τ axis. During the mixing time T, the experiment allows density matrix changes ($\rho_{ee'}$ or $\rho_{gg'}$) to evolve on the ground or excited electronic state. A weakness of these diagrams for 2D relaxation spectroscopy is that they do not show population or coherence transfer during this time interval (although this can be included in the response functions). The detection time t probes coherent dipole radiation, and Fourier transformation of the radiated field with respect to t yields the ω_t axis.

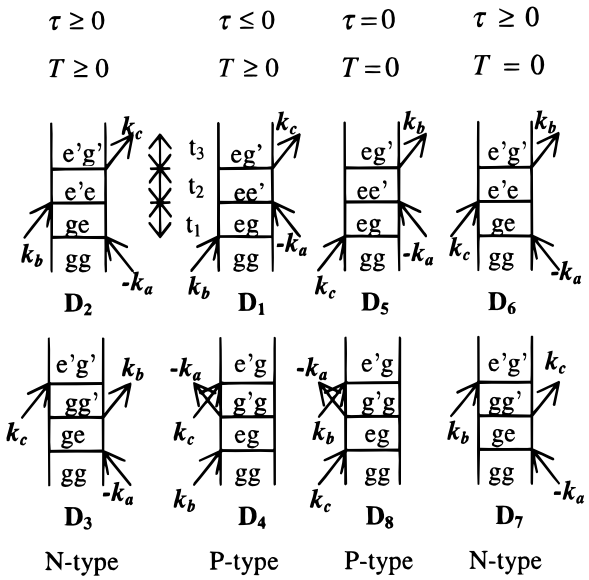

Figure 2. Eight double-sided Feynman diagrams for a two electronic state system which survive the rotating wave approximation and yield a third order polarization with wavevector $(-\boldsymbol{k}_a + \boldsymbol{k}_b + \boldsymbol{k}_c)$. Time increases vertically from bottom to top and t_1, t_2, and t_3 label positive time intervals between field−matter interactions. Incoming diagonal arrows (head touching diagram bar) represent absorption amplitude, while outgoing diagonal arrows (head pointing away from bar) represent emission amplitude. The vertical bars represent the ket (left bar) and bra (right bar) indices of the density matrix element, which changes at each interaction time (horizontal tiebars). The letters in the center of each diagram represent the element of the density matrix probed during that time interval. The time ranges for τ and T at the top indicate when the two diagrams below contribute to the signal for delta-function pulses. Finite duration pulses allow the zeroes in these ranges to be replaced by either $\pm t_p$, where t_p is the pulse duration. The labels at the bottom of each pair indicate whether density matrix element frequencies during t_1 and t_3 are approximately opposite in sign (N-type coherence paths or rephasing diagrams) or approximately equal (P-type coherence paths or nonrephasing diagrams).

Detecting the signal in a particular direction selects the *relative* sign of electronic frequencies observed during τ and t. When the relative sign is negative (N-type coherence pathway), equal and opposite frequency evolution during τ and t will rephase an ensemble of dipoles which oscillate at different frequencies at $t = \tau$, producing a "photon echo".[47] Diagrams D_2, D_3, D_6, and D_7 have N-type coherence pathways[2] and contribute to macroscopic dipole rephasing. When the relative sign is positive (P-type coherence pathways[2] in diagrams D_1, D_4, D_5, and D_8), macroscopic rephasing of an inhomogeneous ensemble is not detected.

$\hat{S}^{(3)}_{rw}$ is given by a pair of functions R_i which depend on the ordering of τ_a, τ_b, and τ_c and is determined by the pair of applicable double-sided Feynman diagrams in Figure 2. Within the rotating wave approximation, expressions for the R_i have been obtained for several relaxation models by Mukamel and co-workers.[36,48] The key quantities in these treatments are the transition frequency correlation function $M(t)$, the reorganization energy λ, the coupling strength Δ, and the line-shape function $g(t)$. The model calculations presented here are based either on a two-level Bloch model or the Brownian oscillator model of Yan and Mukamel.[49] The Brownian oscillator response functions R_i obtained by Yan and Mukamel in terms of the lineshape function $g(t)$ (eq 8.15 of ref 36) are valid in the high-temperature limit $\hbar\omega < kT$ where ω is the oscillator frequency.[50,51] A number of finite pulse duration calculations of femtosecond three pulse scattering signals using these response functions have been published.[35,52,53] Equation 8 differs from these earlier calculations only by using envelope pulse delays instead of carrier wave delays. This difference affects the phase of the signal (hence the 2D spectrum calculated here) but not the intensities measured in the earlier studies.

A systematic analysis of the molecular factors which determine the phase of the nonlinear polarization and radiated signal field in the weak excitation limit is given elsewhere,[43] but the results will be briefly summarized here. It was found that the phase of the signal field is determined by the excitation pulse phases, the time scale of the nonlinear polarization decay, the product of four transition dipole matrix elements, and a pulse delay dependent phase modulation at the frequency of the first dipole oscillation in the four-wave mixing process. Even with perfect phase matching, the emitted field $E_{sig}(t)$ can have some rather complicated dynamics (temporal phase shifts, chirp, envelope distortions) created through the spontaneous radiation by the nonlinear polarization. A Fourier decomposition[43] of the differential equation connecting the nonlinear polarization to the emitted field[36,45,54] shows that

$$\hat{E}_{sig}(\omega_t) = \frac{l}{n(\omega_t)c} i\omega_t \hat{P}^{(3)}(\omega_t) \tag{9}$$

for the perfectly phase-matched case. In eq 9, l is the sample length, n is the refractive index, and c is the speed of light. The product $\hat{F}(\omega_t,\tau,T) \equiv i\ \mathrm{sign}(\omega_t)\ \hat{P}^{(3)}(\omega_t,\tau,T)$ can be easily recovered from experimental data as $\hat{E}_{sig}(\omega)n(\omega)/|\omega|$ and removes the complex radiation dynamics from the 2D spectra while retaining its symmetry with respect to ω_t.[43] Since the spontaneous radiation dynamics are not present in the indirectly detected dimension, this procedure treats both frequency axes in a symmetrical way, preserving the symmetry of a homogeneously broadened 2D line shape. The 2D spectrum is defined by inverse Fourier transformation of $\hat{F}(\omega_t, \tau, T)$ with respect to τ:

$$S_{2D}(\omega_t,\omega_\tau,T) \equiv \int_{-\infty}^{\infty} \hat{F}(\omega_t,\tau,T) \exp(i\omega_\tau\tau)\, d\tau \tag{10}$$

Using $\hat{F}(\omega_t, \tau, T) \equiv \hat{F}(-\omega_t, \tau, T)^*$, it is straightforward to show $S_{2D}(\omega_t,\omega_\tau,T) = S_{2D}(-\omega_t,-\omega_\tau,T)^*$ so that knowledge of S_{2D} on half of the (ω_t, ω_τ) plane is sufficient to characterize the 2D spectrum. For delta function pulses, the real and imaginary parts of 2D electronic spectra obey a Kramers−Kronig relationship with respect to ω_t. Since Kramers−Kronig relates real and imaginary parts over the entire frequency axis, this relationship does not generally hold for finite bandwidth pulses. This Kramers−Kronig relationship arises because the signal is causal with respect to t (no signal before $t = 0$ for delta function pulses). Unlike 2D NMR,[2] there is no Kramers−Kronig relationship for ω_τ. The viewpoint that the Fourier transform with respect to τ separates the frequency domain signal field according to the initial frequency which caused it suggests that the integral of the 2D signal over ω_τ should equal the $\tau = 0$ frequency domain signal field. The $\phi = 0$ case of the projection-slice[55] or projection-cross-section[56] theorem confirms this conjecture, providing a useful connection between 2D spectra and the transient grating field ($\tau = 0$ three pulse scattering signal field)

$$\int_{-\infty}^{\infty} S_{2D}(\omega_t,\omega_\tau,T)\, d\omega_\tau = i\ \mathrm{sign}(\omega_t)\ \hat{P}^{(3)}(\omega_t,\tau{=}0,T) \tag{11}$$

This result says the integral of the 2D spectrum over ω_τ (projection of the 2D spectrum onto the ω_t axis) is equal to the Fourier transform of the time domain transient grating field ($\tau = 0$ data slice) at the same value of T. In a spectrally resolved pump−probe experiment, the signal is the change in transmitted probe spectrum induced by a noncollinear pump.[19−21] For identical transform limited excitation pulses, the real part of the transient grating field $\hat{E}_{TG}(\omega_t)$ is closely related to the spectrally resolved pump−probe signal ΔI_{pp}

$$\Delta I_{pp}(\omega_t) \propto \hat{E}_{TG}(\omega_t)^*\, \hat{E}_{pr}(\omega_t) + \hat{E}_{TG}(\omega_t)\, \hat{E}_{pr}(\omega_t)^* \tag{12}$$

Since $t = 0$ is defined by the center of pulse c in a transient grating experiment and by the center of the probe pulse in a pump−probe experiment, a transform-limited probe pulse has a real frequency domain field $\hat{E}_{pr}(\omega)$ (up to a constant phase which also appears in $\hat{E}_{TG}$ (ω) and therefore cancels). When multiplied by the probe spectral filter, the real part of the 2D projection is equal to the spectrally resolved pump−probe signal

$$\Delta I_{pp}(\omega_t) = \mathrm{Re}[\hat{E}_{pr}(\omega_t) \int_{-\infty}^{\infty} S_{2D}(\omega_t,\omega_\tau,T)\, d\omega_\tau] \tag{13}$$

Since the spectrally resolved pump−probe signal is unaffected by constant phase shifts of either the pump or probe, this relationship should be useful in phasing experimental 2D spectra to correct for interferometer imperfections.

To avoid mixing absorption and dispersion mode 2D spectra, it is necessary to superpose equally weighted signals with equal and opposite "orders of coherence" during the dipole evolution period.[2] The Fourier transform procedure must also be chosen to match the experiment in order to avoid inadvertent Kramers−Kronig transformation between absorption and dispersion mode spectra. For example, a truncated $[0,\infty)$ Fourier transform of the symmetric double-sided interferogram generated by a Fourier transform absorption spectrometer[57] places the Kramers−Kronig transform of the transmitted pulse spectrum into the imaginary frequency spectrum.[38] Hybl et al.[1] scanned continuously across $\tau = 0$ at fixed T, and used complex Fourier transformation over the range $-\infty < \tau < \infty$. A nonlinear optical definition for order of coherence is proposed here in order to examine this procedure in more detail.

In magnetic resonance, the order of coherence p during each time interval between field−matter interactions is defined by $p = \Delta M$, where ΔM is the difference in magnetic quantum number M between states in the coherent superposition.[2] Because of the $\Delta M = \pm 1$ dipole selection rule for circularly polarized radiation, ΔM is uniquely determined by the difference between the number of right and left circularly polarized photons required to conserve angular momentum in a transition. There is no molecular quantity analogous to ΔM for electronic excitation with linearly polarized light. In magnetic resonance, the order

of coherence is operationally selected for by a process called phase cycling: if all the pulses used to prepare a coherent superposition are phase shifted by ϕ, then the signal will be phase shifted by $p\phi$.[58] Provided the spectrum of the pulses does not extend to zero frequency so that phase shifts can be defined as constant changes in the spectral phase,[38] this operational definition of the order of coherence can be extended to nonlinear optics. In time-resolved nonlinear optics, it is well-known that the pulse ordering and macroscopic phase-matching direction for noncollinear beams can be used to selectively probe a reduced set of density matrix elements during each interval between pulses.[36,45] It is shown here that the set of density matrix elements probed during each time interval has a single operationally defined order of coherence for fully noncollinear pulses. If a sample is excited by noncollinear pulses with wave vectors $\boldsymbol{k_i}$ and a perfectly phase matched nonlinear signal is detected with wave vector $\boldsymbol{k_s} = \sum s_i \boldsymbol{k_i}$ where $s_i = \pm 1$, then constant spectral phase shifts ϕ_i of the excitation pulses yield a phase shift of the signal given by $\phi_s = \sum s_i \phi_i$.[33,38] This implies that the operational order of coherence[58] after the jth excitation pulse in a nonlinear optical experiment is given by

$$p_j = \sum_{i=1}^{j} s_i \tag{14}$$

If all the excitation pulses are noncollinear and temporally nonoverlapping, the order of coherence during each interval between pulses is uniquely determined by the phase matching direction and the time ordering of the pulses. Unlike ΔM, the operational order of coherence in nonlinear optics is not an obviously conserved quantity between pulses. Linearity of the Liouville equation[36,59] suggests the operational order of coherence is conserved in the sense that the spatial dependence $\exp[i\sum_i s_i \boldsymbol{k}_i \cdot r]$ of density matrix elements is preserved. Relaxation models which retain linearity for subsystems[59,60] will conserve the operational order of coherence between pulses.

Examining the double-sided diagrams in Figure 2 shows that in the four-wave mixing experiments treated here, the order of coherence during the evolution period after the first interaction can be either $p_1 = -1$ if pulse a interacts first (diagrams D_2, D_3, D_6, and D_7) or $p_1 = +1$ if pulse b (diagrams D_1 and D_4) or c (D_5 and D_8) interacts first; after the second interaction, $p_2 = 0$ during the mixing period; and $p_3 = +1$ during the detection period after the third interaction. (Only the relative signs of p_j during different time intervals are significant as a change of all signs corresponds to complex conjugation.) This establishes that the coherence transfer pathways[2] in EASY 2D electronic spectroscopy are identical to those in the simplest implementations of NOESY 2D NMR (nonzero T) and COSY 2D NMR (for $T = 0$). The problem of equally weighting the opposite orders of coherence $p_1 = +1$ and $p_1 = -1$ during the evolution period will now be addressed. Hybl et al.[1] scanned continuously across $\tau = 0$ and used complex Fourier transformation over the range $(-\infty, \infty)$ for both t and τ. N-type coherence paths[2] with $p_1 = -1$, $p_2 = 0$, $p_3 = +1$ can produce macroscopic dipole rephasing and a real photon echo signal.[61] P-type coherence paths with $p_1 = +1$, $p_2 = 0$, $p_3 = +1$ cannot rephase (these signals are called virtual photon echoes[61] or "antiecho" in NMR[2]). The procedure adopted by Hybl et al.[1] effectively superposes P-type signals (which dominate for negative τ) and N-type signals (which dominate for positive τ) with the inverse Fourier transformation over all τ.

For T greater than the pulse duration, only properly time ordered double-sided Feynman diagrams D_1-D_4 contribute to the signal, and the rephasing (N type) diagrams which contribute for positive τ are balanced by nonrephasing (P type) diagrams which contribute for negative τ. Equal and opposite orders of coherence are equally weighted so that scanning across $\tau = 0$ produces real 2D absorption and imaginary 2D dispersion peak shapes. The improperly time ordered diagrams contribute to the signal if T is less than the pulse duration. The improperly ordered diagrams may be unbalanced: the nonrephasing (P type) diagrams D_5 and D_8 contribute only when all three pulses overlap while the rephasing (N type) diagrams D_6 and D_7 can also contribute for nonoverlapping positive τ less than the dephasing time. For T less than the pulse duration, the procedure of scanning across $\tau = 0$ does not equally weight opposite orders of coherence. A partially "phase twisted" peak shape[2] which mixes absorption and dispersion lineshapes in the 2D spectrum can result from this imbalance in a two-level system. This problem increases in importance for shorter pulses, which preferentially reduce the contribution from the nonrephasing improperly time ordered diagrams. However, for sufficiently short pulses, setting T greater than the pulse duration could eliminate this imbalance without missing any dynamics.

There is also a more subtle source of possible N/P imbalance. When each electronic state contains two sublevels, every double-sided Feynman diagram yields eight distinct energy ladder subdiagrams for each level of the ground state. Figure 3 shows the eight subdiagrams which start in the upper sublevel of the ground state for the properly ordered excited state double-sided diagrams D_1 (nonrephasing) and D_2 (rephasing). In energy ladder diagrams, arrows on the right side of the double-sided diagrams are solid, while arrows on the left side of the double-sided diagrams are dashed. Time runs from left to right, and the signal radiation is shown as a wavy line. The rules for these diagrams have been summarized by Lee and Albrecht.[62]

When the eight rephasing subdiagrams are compared to the corresponding eight nonrephasing subdiagrams, the first four subdiagrams in each set exhibit a rephasing/non-rephasing balance. In general, the first two subdiagrams represent a reduction in absorption (in $1d_1$ and $1d_2$, excited state population leads to stimulated emission and a transmission increase at the initial excitation frequency). The next two subdiagrams represent double resonances (in $1d_3$ and $1d_4$, excited state population leads to stimulated emission at a different frequency). The ground state versions of these four subdiagrams involve ground state depopulation reducing the absorption on every transition out of the depopulated level. In optics, subdiagrams d_3 and d_4 are known as "V" (common ground state) or "Λ" (common excited state) double resonances based on the energy level diagram.[63] In NMR, subdiagrams d_3 and d_4 correspond to "regressive transitions" which yield pure 2D absorption peakshapes in weakly coupled spin systems.[2]

In contrast, the four subdiagrams which involve coherent sublevel excitation (d_5-d_8) may be imbalanced. Two of the four subdiagrams (d_7 and d_8) which involve coherent sublevel excitation have transition dipole products of the type $\mu_{ab}\mu_{bc}\mu_{cd}\mu_{da}$, which must be real but may be either positive or negative.[43] The other six subdiagrams (d_1-d_6) have transition dipole products of the real and positive form $|\mu_{ab}|^2|\mu_{bc}|^2$. The two subdiagrams which can have negative transition dipole products (d_7 and d_8) correspond to "parallel transitions" which yield 2D peaks of either sign[64,65] with mixed absorption/dispersion peak shapes in strongly coupled spin systems.[2] The radiation produced by these parallel transitions can lie outside the spectrum of the excitation pulses. Since four different frequencies are involved, these parallel four-wave mixing transitions may not appear in

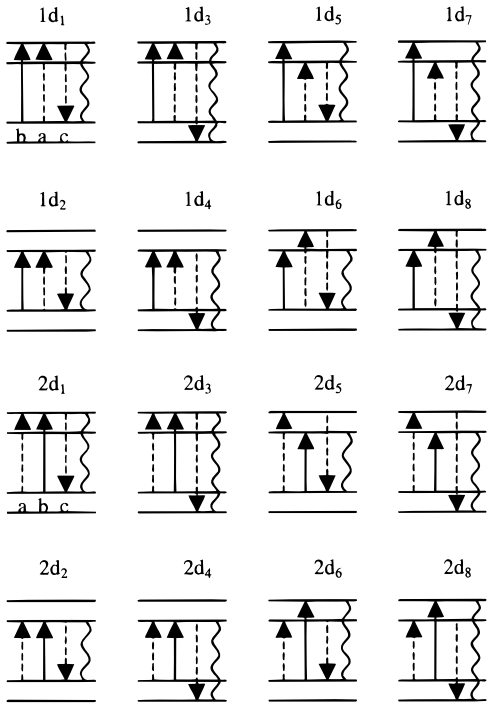

Figure 3. Energy ladder subdiagrams for double-sided Feynman diagrams D_1 (above) and D_2 (below). Only the eight subdiagrams starting from the upper sublevel of the ground electronic state are shown. D_1 and D_2 are the properly ordered diagrams which evolve on the excited state during the population period (see Figure 2). D_1 is nonrephasing (P-type coherence) and contributes primarily for negative τ while D_2 is rephasing (N-type coherence) and contributes primarily for positive τ. For both D_1 and D_2, subdiagrams d_1-d_4 show excited state emission in Λ type double resonances. The two sets of subdiagrams d_1-d_4 are in exact correspondence with respect to the initial frequency, density matrix element probed during the time interval t_2, and density matrix element probed during t_3 (hence radiated frequency). The only difference is the type of coherence (N for D_2 vs P for D_1) probed during t_1, so that subdiagrams d_1-d_4 are in rephasing/nonrephasing balance and will yield real 2D absorption line shapes for all T. In contrast, the two sets of subdiagrams d_5-d_8 which involve coherent superposition states after the second interaction cannot even be paired so the initial and final frequencies match. The two sets of subdiagrams d_5-d_8 have a dephasing/rephasing imbalance and may produce "phase-twisted" line shapes. In both sets of subdiagrams d_1-d_6, every transition dipole appears also in complex conjugate form so that the product of four transition dipole moments is real and positive. Subdiagrams d_7 and d_8 involve four different transition dipole moments and their product can be either a positive or negative real number. If the transition dipole product is negative, these subdiagrams can contribute negative intensity peaks to the 2D spectrum.

non-FT 2D spectra assembled by combining pump-probe signals.[12] The division of the eight energy ladder subdiagrams into four balanced double resonance diagrams plus 4 imbalanced coherent sublevel excitation diagrams and the division into six positive signal diagrams plus two possibly negative subdiagrams discussed above both hold generally in the absence of relaxation. It seems likely that some relaxation processes (e.g. generation of coherent vibrational wavepackets by rapid internal conversion[17]) can produce negative signals not considered above. The rephasing/nonrephasing imbalance produced by these coherent processes in a multilevel system might yield phase-twisted 2D peaks even when the improperly ordered diagrams cannot contribute to the signal. Such phase twisted peaks will not occur after sublevel coherences decay (i.e. when T greatly exceeds the vibrational T_2).

III. Calculations

In eq 8, setting $\omega_0 = \omega_a = \omega_b = \omega_c$ and pulling the t_a and t_b delay dependent field oscillations outside the integral along with the t dependent oscillation yields

$$P^{(3)}(\boldsymbol{k}_{sa},t,t_a,t_b) = \exp[i\omega_0(t-\tau)] \times \int_0^\infty \int_0^\infty \int_0^\infty \hat{S}^{(3)}_{rw}(\boldsymbol{k}_{sa},\tau_a,\tau_b,\tau_c) \exp[i\omega_0(-\tau_a+\tau_b+\tau_c)] \times \hat{e}^*_a(t-t_a-\tau_a)\hat{e}_b(t-t_b-\tau_b)\hat{e}_c(t-\tau_c)\, d\tau_a\, d\tau_b\, d\tau_c + \text{complex conjugate} \quad (15)$$

where $\tau \equiv t_b - t_a$. The reference frequency ω_0 in the complex field can be chosen to match the electronic Bohr frequency ω_{eg} so that τ_α dependent oscillations in $\hat{S}^{(3)}_{rw}$ are cancelled by the exponential adjacent to it in eq 15. Provided the reference frequency is not too different from the pulse center frequency, one obtains the sort of slowly oscillating complex integral expected from the rotating wave approximation.

The sum of the explicitly written integral and its complex conjugate in eq 15 is rapidly oscillating in both t and τ, which would require a high Nyquist sampling rate (two points per cycle of the highest frequency)[66] for the double Fourier transformation. A much lower sampling rate (one point per cycle of the spectral bandwidth) can be used to Fourier transform only the explicitly written triple integral in eq 15, which yields a 2D spectrum centered at $\omega_t = \omega_{eg} - \omega_0$, $\omega_\tau = -(\omega_{eg} - \omega_0)$. After Fourier transformation of the slowly varying triple integral, the rapidly oscillating $\exp[i\omega_0(t-\tau)]$ term is included using the Fourier shift theorem[66] by addition and subtraction of ω_0 from ω_t and ω_τ, respectively. This recenters the 2D spectrum at $\omega_t = \omega_{eg}$, $\omega_\tau = -\omega_{eg}$. The contribution of the complex conjugate term in eq 15 to the 2D spectrum is obtained by inverting both frequency axes. This procedure saved an order of magnitude in computing time by reducing the number of triple integrals required to do the 2D Fourier transform. This undersampling of a phase-modulated signal does not overlap different 2D peaks, so phase cycles[3] are not required to separate them. Undersampling τ without phase cycling should also be possible in the EASY 2D experiment.

In numerical calculations, the interaction times τ_α in the triple integrals ranged over $(t - t_a) \pm 2.5t_p$, where t_p is the Gaussian pulse duration. The three integrals over τ_α were computed using the Numerical Recipes Gauss−Legendre quadrature routine gauleg.f.[67] Six quadrature points for each nearly Gaussian integral typically sufficed for convergence (this rapid quadrature algorithm was generously provided by Dr. Jae-Young Yu). A series of time domain calculations of third-order nonlinear optical signals used to check the code are described elsewhere.[43,68] The Fourier transform variable t ranged from $-2.5t_p$ to t_{max}; τ ranged from $-\tau_{max}$ to τ_{max}.

As a check on the 2D Fourier transformation, optical Bloch model 2D spectra were calculated using pulse durations of 0.1 fs, and step sizes of 1 fs in both t and τ for comparison to the analytical expression for this signal in the impulsive limit. Since NMR signals are often described in this limit, there is a vast literature describing the resulting line shapes.[2,3] For $t \geq 0$, the third-order polarization of a two-level system in the optical Bloch limit is given by

$$P^{(3)}(t,\tau,T) = \exp[-\Gamma(t+|\tau|)] \exp[-T/T_1] \times \sin[\omega_{eg}(t-\tau)][1+\delta(T)\theta(\tau)] \quad (16)$$

where ω_{eg} is the electronic transition frequency, Γ is the dipole decay rate ($1/T_2$), and T_1 is the population grating lifetime. There

is no phase-matched third-order polarization before pulse *c* hits the sample at $t = 0$. $P^{(3)}$ then oscillates, with the oscillation decaying exponentially in t. Dipole decay before the arrival of the second pulse causes an exponential decay of $P^{(3)}$ with the delay $|\tau|$. Dipole oscillation during τ modulates the initial phase of the oscillating third-order polarization. For $T = 0$, there is a discontinuity in the nonlinear polarization at $\tau = 0$ where it instantly increases by a factor of 2 for positive τ (hence the $\delta(T)\ \theta(\tau)$ term where $\theta(\tau)$ is the Heaviside unit step function and $\delta(0) = 1$ but is otherwise zero). This jump was not included in eq 1 of ref 1 which is valid only for $T > 0$.

The impulsive 2D electronic spectrum in the Bloch limit is given by

$$\begin{aligned} S_{2D}(\omega_t,\omega_\tau,T) = a(-\omega_\tau)a(\omega_t) - \mathrm{i}a(-\omega_\tau)d(\omega_t) + \\ (1/2)\delta(T)[a(-\omega_\tau)a(\omega_t) + d(-\omega_\tau)d(\omega_t) - \\ \mathrm{i}a(-\omega_\tau)d(\omega_t) + \mathrm{i}d(-\omega_\tau)a(\omega_t)] + \\ a(\omega_\tau)a(-\omega_t) + \mathrm{i}a(\omega_\tau)d(-\omega_t) + \\ (1/2)\delta(T)\ [a(\omega_\tau)a(-\omega_t) + d(\omega_\tau)d(-\omega_t) + \\ \mathrm{i}a(\omega_\tau)d(-\omega_t) - \mathrm{i}d(\omega_\tau)a(-\omega_t)] \quad (17) \end{aligned}$$

where

$$a(\omega) = \frac{\Gamma}{(\omega_{eg} - \omega)^2 + \Gamma^2}$$

$$d(\omega) = \frac{(\omega_{eg} - \omega)}{(\omega_{eg} - \omega)^2 + \Gamma^2} \quad (18)$$

are one-dimensional Lorentzian absorptive and dispersive lineshape functions.[2] The 2D spectrum is nonzero only in two symmetry related quadrants. The calculated $T = 0$ 2D spectrum in Figure 4a demonstrates a partial "phase twist"[2,3] caused by the imbalance between rephasing and nonrephasing contributions to the 2D spectrum in the $\delta(T)\theta(\tau)$ term. The $\delta(T)$ term in the spectrum is known as a phase-twisted line shape in 2D NMR.[2,3] Once T exceeds the pulse duration at $T = 2$ fs, this partial twisting is gone (Figure 4b) and the 2D spectrum does not change shape with T. For $T > 0$, the 2D Bloch spectrum has real and imaginary parts with Lorentzian absorptive and dispersive line shapes. The real part of the 2D spectrum is a product of two absorption line shapes with a characteristic star shape[1−3] while the imaginary part is the product of an absorption lineshape in ω_τ and a dispersion line shape in ω_t with a nodal line at $\omega_t = \omega_{eg}$.[1] The real absorptive and imaginary dispersive line shapes in ω_t result from scattering off an electronic state population grating which creates both absorption coefficient and refractive index gratings.[37]

Since 2D spectra are additive, an inhomogeneous distribution $p(\omega_{eg})$ of Bohr transition frequencies, ω_{eg}, will elongate the spectrum in eq 17 by convolution with $p((\omega_t - \omega_\tau)/\sqrt{2})\delta((\omega_t + \omega_\tau)/\sqrt{2})$ to produce a positive ridge along the diagonal.[1] This is the 2D spectrum for an inhomogeneous ensemble of two-level systems with Lorentzian line shapes due to a static distribution of local chromophore environments (e.g. low-temperature glasses). The Bloch model cannot account for the time-dependent local environment in solution very well, because the dynamics cannot be cleanly split into infinitely fast (homogeneous) and infinitely slow (inhomogeneous) processes. In condensed phases, the response function should include spectral diffusion and the Stokes' shift. The Brownian oscillator response functions of Yan and Mukamel[36,49] produce 2D spectra that are clearly inhomogeneously broadened near $T = 0$ (before different local environments can interconvert) and gradually become homogeneously broadened with increasing T as local environments lose memory of their initial configuration. Vibrational sublevel relaxation not shown in the diagrams is included semiclassically. The Brownian oscillator model includes both spectral diffusion and the Stokes' shift, explicitly forces all electronic dephasing processes to arise from nuclear motion on finite time scales, and treats the difference between homogeneous and inhomogeneous broadening as simply a matter of time scale rather than a difference in mechanism.[36]

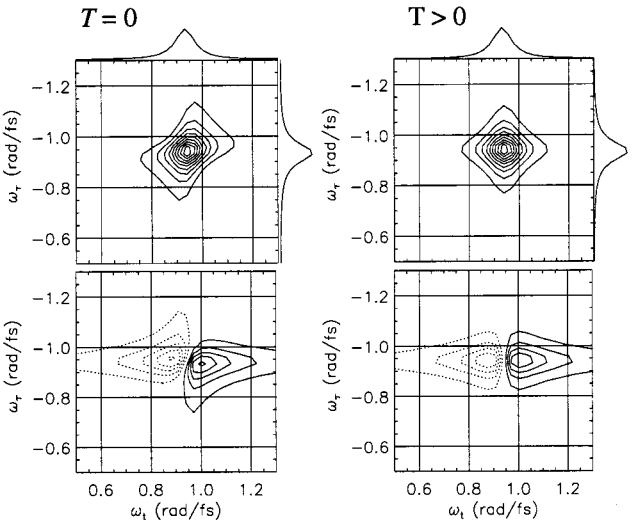

Figure 4. Impulsive two-dimensional spectra for the Bloch model with $\Gamma = 300\ \mathrm{cm}^{-1}$. The 2D spectra on the left (a) were calculated for $T = 0$, and the 2D spectra on the right (b) for $T = 2$ fs. The upper plots show the real (absorptive) part of the 2D spectrum and the lower plots show the imaginary (dispersive) part of the 2D spectrum. The vertical axis ω_τ is the indirectly detected frequency of dipole oscillation during the evolution period. The horizontal axis ω_t is the directly detected frequency of the emitted signal field during the detection period. Contour intervals are 10% of the real maximum. Dotted contours are negative. The spectra on the top and right axes are the integral of the signal over the other axis. On the left, the overlap between pulse c and a or b during a $T = 0$ scan gives rise to a partially "phase-twisted" 2D spectrum because of a rephasing/nonrephasing coherence imbalance (see text). All Bloch model 2D spectra are identical to that on the right once pulse c no longer overlaps either a or b during the scan. For $T > 0$, the absorptive (real) spectrum is a two-dimensional Lorentzian $a(-\omega_\tau)a(\omega_t)$ and the dispersive (imaginary) spectrum is the product of Lorentzian absorption and dispersion line shapes $a(-\omega_\tau)d(\omega_t)$.

IV. Results

A goal of these simulations is to understand how different processes in the electronic dynamics of molecules in solution are manifested in 2D spectra. There is no clear dividing line between the solute and a strongly interacting solvent. Distinction between intramolecular and solvent motions is not possible without comparisons between related solute/solvent systems. Molecules in solution usually have some underdamped vibrations present in all solvents, some coupling to motions seen in spectra of the neat solvent, and some damped vibrations of less certain origin.[69] Of particular interest is inertial solvation,[15,70] the earliest step in polar solvation when the solvent takes time to react to the new solute charge distribution. Here the electronic frequency correlation function $M(t)$ is expected to decay initially as $1 - \beta t^2$ which is often extended as a Gaussian.[70] Even experiments using short pulses (10−20 fs) have not been able to characterize the short-time behavior of the frequency correlation function $M(t)$ in some solvents, and there has been

TABLE 1: Bohr Frequency Correlation Functions

$M(t)$	equation	use
overdamped Brownian oscillator[a]	$M(t) = (s_+/(s_+ - s_-)) \exp(-s_- t) - (s_-/(s_+ - s_-)) \exp(-s_+ t)$	inertial solvation
critically damped Brownian oscillator	$M(t) = \exp(-\gamma t/2)[1 + \gamma t/2]$	inertial solvation
Gaussian	$M(t) = A \exp(-t^2/\tau_g^2)$	inertial solvation
decaying exponential	$M(t) = A \exp(-t/\tau_c)$	picosecond solvation dynamics
underdamped Brownian oscillator[b]	$M(t) = \exp(-\gamma t/2)[\cos(\omega' t) + (\gamma/2\omega') \sin(\omega' t)]$	intramolecular vibrations
damped cosinusoid	$M(t) = A \exp(-t/\tau_c) \cos(\omega t + \phi)$	intramolecular vibrations

[a] Overdamped oscillator exponential coefficients $s_\pm = \gamma/2 \pm [(\gamma/2)^2 - \omega^2]^{1/2}$. [b] Underdamped oscillator reduced frequency $\omega' = [\omega^2 - (\gamma/2)^2]^{1/2}$.

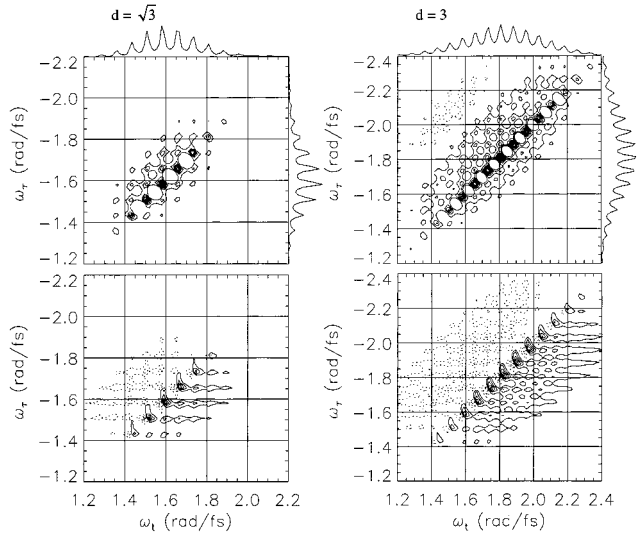

Figure 5. Real and imaginary 2D correlation spectra at zero mixing time ($T = 0$) for underdamped Brownian oscillators with a vibrational frequency $\omega = 400$ cm^{-1} at a temperature of 800 K. (a, left) $d = \sqrt{3}$, $\omega_{eg} = 8000$ cm^{-1}, $\gamma = 10$ cm^{-1}. (b, right) $d = 3$, $\omega_{eg} = 8000$ cm^{-1}, $\gamma = 5$ cm^{-1}. With an increase in the displacement d between the upper and lower states, there is an increase in the number of vibrational states excited. Calculations which include only ground state or only excited state response functions both yield exactly the same 2D spectrum. Each electronic state contributes half of the total 2D intensity.

disagreement over whether there is evidence for inertial solvation in photon echo measurements on dyes in solution.[35,71,72] It is useful to calculate 2D spectra for the limiting cases of the Brownian oscillator and several other functions commonly used in approximating the transition frequency correlation function $M(t)$ in order to understand their effect on the overall measured signal. Representative 2D spectra for the various parts of $M(t)$ listed in Table 1 were calculated and analyzed to gain insight into their respective roles in solvation processes. Since finite bandwidth pulses simply acted as a spectral filter, 2D spectra were calculated with impulsive pulses to view the widest bandwidth in the frequency spectra unless otherwise noted. These impulsive 2D spectra obey a Kramers−Kronig relation with respect to ω_t, which was used as an additional check on the calculations.

IVA. Underdamped Oscillator. Perhaps the most illuminating case in Table 1 for understanding 2D electronic spectroscopy, if not the most relevant to solvation dynamics, is the underdamped Brownian oscillator. The damped cosinusoid shows essentially the same behavior, so this discussion will be limited to the underdamped oscillator. An underdamped oscillator repeatedly oscillates before relaxing to a thermal equilibrium coordinate distribution near the bottom of the excited state potential energy surface, completing its Stokes' shift. For a Brownian oscillator, all vibrational phase relaxation is caused by vibrational energy loss. Figure 5 shows mixing time $T = 0$ real and imaginary spectra for two differently displaced oscillators with frequency $\omega = 400$ cm^{-1} at a temperature of 800 K. The oscillator vibrational motion has a period of 83 fs and an exponential damping time of 1060 fs. Because of the repeated oscillation, discrete peaks can be seen in the 2D spectrum. The repeated oscillations of the underdamped oscillator were calculated on 150 unevenly spaced Gaussian quadrature points in t; cubic splines were used to interpolate onto a 512-point evenly spaced grid for the FFT. This Fourier-transformed signal was calculated at 256 values of τ and the resulting array was transformed with respect to τ. The spectra in Figure 5a (left) have dimensionless displacement of the excited state minimum from the ground state minimum, $d = \sqrt{3}$. ($d = \sqrt{2\lambda/\omega}$, where λ is the reorganization energy and ω is the oscillator frequency.) Figure 5b (right) shows a spectrum with $d = 3$. In the real spectra (top row) the one-dimensional spectra lining either axis are the result of integrating the signal over the other axis (projected spectra). For $T > t_p$, the 2D projection onto ω_τ *resembles* a filtered absorption spectrum in the calculations performed so far. Outside the models used for calculation, such a relationship depends on the relaxation dynamics of the system (e.g. breakdown occurs for internal conversion rates which depend on the vibrational energy). For delta function pulses, the projection of the 2D spectrum onto ω_t is equal to the spectrally resolved pump−probe signal (see eq 13).

The *same* 2D correlation spectrum is observed when the calculation is restricted to include only excited state response functions or only ground state response functions. The negative region persists for nonzero mixing time T, but is not present for nonzero T in an inhomogeneously broadened two-level Bloch model. The negative region of the projection and the negative peaks in the 2D spectrum that lead to it are evidently related to coherent wavepacket excitation on either the ground or excited electronic states during the second and third pulses. Off-diagonal energy level subdiagrams like $1d_8$ and $2d_8$ in Figure 3 can produce negative intensity peaks in a 2D spectrum if they have a negative transition dipole product. Analysis of a four-level system suggests these negative subdiagrams tend to yield stronger 2D peaks for $\omega_t < \omega_\tau$ when lower energy sublevels of the ground electronic state are preferentially populated. The proportion of possibly negative intensity subdiagrams increases with the number of sublevels.

The negative regions of the ground state 2D spectrum may be related to stimulated Raman excitation of wavepackets on the ground state. A similar effect has been predicted for pump−probe transients, where the enhanced vibrational amplitude produces increased ground state absorption in the wings of the steady-state absorption, although the negative signals are masked except at low temperature.[73] Although a single δ-function pulse cannot excite ground state wavepackets within the Condon approximation used in the Brownian oscillator model, a δ-function pulse pair can cause stimulated Raman scattering because there is time for wavepacket evolution on the excited state between pulses.[74] The excited state subdiagrams d_7 and d_8 exhibit similar access to possibly unpopulated ground state sublevels. A single "absorption frequency" and "emission frequency" are inadequate to fully describe the 2D spectra when

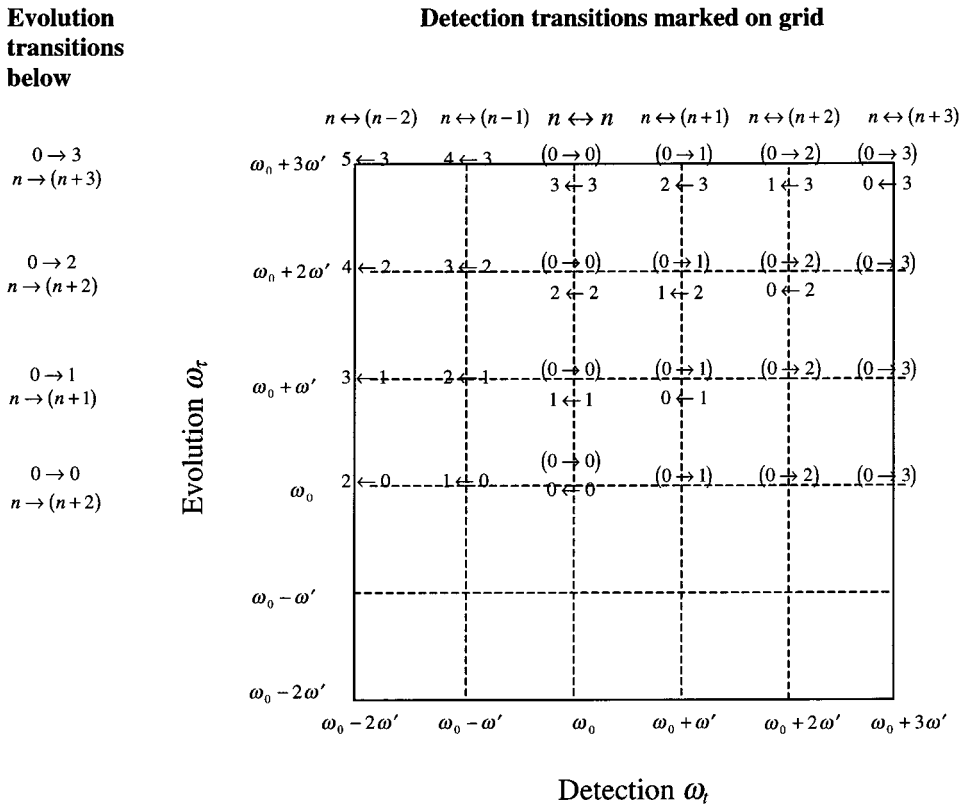

Figure 6. Illustration of the energy levels and peak assignments in the 2D spectrum of an underdamped oscillator. The vertical axis shows excitation frequencies (ω_τ) and the horizontal axis shows detection frequencies (ω_t). These frequencies correspond to the first (leftmost) and last (wavy) Bohr energy differences shown on the sublevel diagrams in Figure 3. At least two sets of labels are necessary to identify a peak: the excitation transition and at least one detection transition (shown at grid intersections). The vibrational quantum number of the ground electronic state is always first. Excitation transitions are marked to the left of the grid and apply to an entire row. Detected transitions are marked directly on the grid. Transitions in parentheses represent detection of ground state bleaches in V type double resonances, while transitions without parentheses represent excited state emission in Λ double resonances. Note that coherent four-level contributions to 2D spectra cannot be described as double resonances, may contribute to the 2D spectrum with either sign, and have excitation and detection transitions which may not share a common level. After vibrational coherence is gone, two sets of levels suffice to identify each peak. In the absence of hot bands, V type bleaching can only occur for $\omega_t \geq \omega_0$ and Λ type stimulated emission can only occur for $\omega_t \leq \omega_\tau$. $\omega_0 = \omega_{eg} + \lambda$; ω' is the reduced oscillator frequency.

wavepackets are created on both electronic states. The full process should be understood at the field/amplitude level. It is rigorously correct to describe the ω_τ frequency as an initial dipole oscillation frequency during the evolution period and the ω_t frequency as the final dipole radiation frequency during the detection period. These frequencies are given by the Bohr frequencies for the first (leftmost) straight arrow (ω_τ) and final wavy line (ω_t) in the energy ladder sub-diagrams of Figure 3.

As in pump−probe spectroscopy,[73] a positive peak in the 2D spectrum indicates a "bleach" (reduction in ground state absorption or increase in excited state emission). Energy ladder subdiagrams d_1−d_4 in Figure 3 produce positive 2D peaks which correspond to pump-induced increases in probe transmission. More generally, the phase of a peak in the 2D spectrum is determined by the phase of the final dipole oscillation relative to the initial dipole excitation. Subdiagrams like d_5 and d_6 produce positive 2D signals, possibly with phase-twisted shapes because of N/P imbalance (note the twisted diagonal peaks in Figure 5). A negative intensity 2D peak suggests increased light absorption in pump−probe and subdiagrams similar to d_7 and d_8 play a role in producing negative peaks seen above the diagonal in Figure 5b.

Vibrational relaxation eliminates sublevel coherences represented by subdiagrams d_5−d_8 and allows a rigorous attribution of real 2D spectra to changes in absorption (and emission) at ω_t caused by previous absorption at ω_τ. Figure 6 shows the assignment of positive vibronic peaks in a 2D relaxation spectrum where the excited state has vibrationally dephased without vibrational population relaxation (vibrational $T_1 \gg T \gg$ vibrational T_2). The vertical axis is the ω_τ axis, labeled at the $0 \rightarrow 0$ frequency, $\omega_0 = \omega_{eg} + \lambda$, plus integer multiples of the reduced oscillator frequency, $\omega' = [\omega^2 - (\gamma/2)^2]^{1/2}$. The horizontal axis, ω_t, is labeled in the same manner. The vibrational quantum number on the lower electronic state is always listed first. At least two sets of labels are required to assign a given peak in the spectrum. The excitation label, listed under "Evolution" in the figure, determines the peak position along the ω_τ axis. The detection label(s), shown at the grid points and labeled "Detection", determine the position along the ω_t axis. For the column labeled ω_0 along the ω_t axis, the ground state bleach signals, labeled in parentheses, overlap the excited state emission signals (no parentheses).

Figure 7 shows a vibrationally relaxed 2D spectrum calculated for mixing time $T = 100$ ps, temperature 800 K, displacement $d = 3.5$, and oscillator frequency $\omega = 400$ cm^{-1}. In contrast to the 2D correlation spectrum in Figure 5, the real 2D relaxation spectrum in Figure 7 is entirely positive and individual peaks do not exhibit any phase twist. In contrast to Figure 6, vibrational population relaxation is complete in Figure 7, so all initially excited levels yield the same level distribution. Labels similar to those in Figure 6 can be used to assign the absorption mode 2D spectrum in Figure 7a. Figure 7b shows the dispersion mode spectrum. The excited state emission spectrum (centered at $\omega_t = \omega_{eg} - \lambda$) and the ground state absorption spectrum (centered

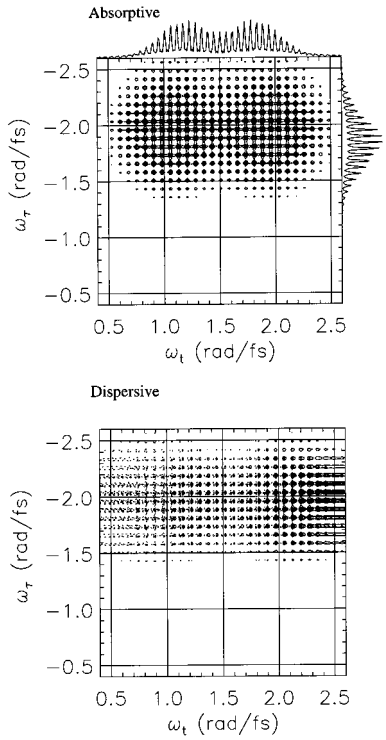

Figure 7. 2D relaxation spectra at mixing time $T = 100$ ps for an underdamped Brownian oscillator with parameters: $d = 3.5$, $\omega_{eg} = 8000$ cm^{-1}, $\omega = 400$ cm^{-1}, $\gamma = 3$ cm^{-1} at a temperature of 800 K. Real 2D absorption spectra are shown on the top; imaginary 2D dispersion spectra are shown on the bottom. The 2D absorption mode spectrum at $T = 100$ ps is a product of the projections onto ω_t and ω_τ, indicating complete relaxation. The oscillator has completely relaxed and the spectrum is symmetrical around $\omega_t = \omega_{eg} = 8000$ cm^{-1} = 1.51 rad/fs. At $T = 100$ ps, each vibronic peak has a line shape reminiscent of the Bloch 2D Lorentzian. Compare to Figure 6 for the peak assignments.

at $\omega_t = \omega_{eg} + \lambda$) are of equal intensity (electronic population relaxation was not included in these calculations). The projected spectrum is the sum of the steady state absorption and emission spectra. Near $\omega_t = \omega_0$, the absorption and emission spectra overlap. The real 2D spectrum is a product of the real projections onto the ω_t and ω_τ axes, and the imaginary 2D spectrum is a product of the real 2D projection onto the ω_τ axis and the imaginary 2D projection onto ω_t. Such product 2D spectra indicate the system is vibrationally equilibrated at mixing time $T = 100$ ps.

Returning to Figure 5 and the $T = 0$ spectra, the main difference between parts a and b is the number of vibrations in the observed progression. Below $\omega_\tau = \omega_0$, there are "hot bands" in the integrated ω_τ spectrum in Figure 5b caused by $n \rightarrow 0$ excitation transitions. Peaks below $\omega_t = \omega_0$ show up in the integrated ω_t spectrum as well, indicating that ($n \rightarrow 0$) hot bands have been bleached. Lowering the temperature to 200 K eliminates these hot bands.[75] One feature that is similar in both spectra in Figure 5 is the difference in signal intensity above and below the diagonal. Since the same 2D spectrum was obtained for the separate ground state and excited state response, this asymmetry cannot be attributed to vibrationally dephased emission only above the diagonal.

Since the mean thermal energy is usually large relative to Zeeman splittings and small relative to the electronic energy gap, temperature creates prominent differences between 2D electronic spectra and their NMR counterparts. 2D NMR spectra are usually symmetric about the diagonal,[2,3] while 2D electronic relaxation spectra have more peaks above the diagonal than below because emission generally lies to the red of absorption (Stokes' rule). As a result, the bulk of the 2D spectrum lies above $\omega_\tau = \omega_{eg}$ and below $\omega_t = \omega_{eg} + \lambda$ in all systems examined here.

2D spectra of the underdamped oscillator provide a detailed picture of the vibrational wavepacket motion. Figure 8 shows real 2D spectra at $T = 0$, 20, 40, 60, and 80 fs, with Brownian oscillator parameters $\omega_{eg} = 10\,000$ cm^{-1}, $d = 3$, $\omega = 400$ cm^{-1}, $\gamma = 10$ cm^{-1}, and a temperature of 600 K. The vibrational period is 83.3 fs. The projection of the 2D spectrum onto the ω_t axis is exactly equal to the spectrally resolved pump−probe signal (eq 12 with δ-function pulses) and reflects wavepacket position vs T. The center of the excited state spectrum oscillates between $\omega_t = \omega_{eg} + \lambda$ ($T = 0$ and 80 fs) and the value of ω_t corresponding to the outer turning point of the wavepacket $\omega_t = \omega_{eg} - 3\lambda$ ($T = 40$ fs) while the ground state spectrum remains centered at its $T = 0$ position. Vibrational coherence produces negative regions in the 2D spectrum that are mostly masked in the projection by positive 2D peaks. At $T = 20$ fs the wavepacket has moved near the middle of the excited state well and the emission peaks near $\omega_t = \omega_{eg} - \lambda$ are clearly visible. Notice the fine band structure perpendicular to the diagonal. At $T = 40$ fs the excited state emission and ground state bleach bands are maximally separated. The reversed 2D tilt of the ground state bleach band (centered at $\omega_t \approx \omega_{eg} + \lambda$) is consistent with absorbers initially at the inner potential wall moving to the outer wall (and vice versa). Similarly, the reversed tilt of the excited state emission band (at $\omega_t \approx \omega_{eg} - 3\lambda$) arises from large-amplitude motion of the entire wavepacket to the other side of the excited state potential. As the wavepacket is returning to the inner turning point at $T = 60$ fs, the excited state spectrum moves in toward the ground state spectrum again and the high momentum band structure returns, but this time oriented along the diagonal. At $T = 80$ fs the wavepacket has returned close to the inner turning point and the spectrum resembles that at $T = 0$, though slightly more spread out. For inhomogeneously broadened electronic bands in solution, the change in overall projected spectra (summed over ω_τ) can reveal vibrational wavepacket position as a function of T by pump−probe methods. The correlation of positions within the wavepacket and differences in the 2D band structure for values of T corresponding to different wavepacket *momenta* are exciting. The momentum-dependent 2D band structure parallel to the diagonal will not be washed away even by severe inhomogeneous broadening, so 2D electronic spectra should be useful for studies of condensed phase wavepacket motion.

IVB. Solvation. For molecules with a significant dipole moment change upon electronic excitation, inertial solvation usually accounts for fifty percent or more of the total Stokes' shift in polar solvents.[14] All three of the functions (overdamped and critically damped Brownian oscillators, and Gaussian in Table 1) used to approximate inertial solvation in $M(t)$ result in qualitatively similar 2D spectra. Although the overdamped oscillator is not a physically reasonable model of inertial solvation in liquids, it has been used in some calculations. 2D spectra of critically damped and overdamped Brownian oscillators with the same oscillator frequency ω are almost indistinguishable by eye. In the real part, the extent of the spectra along the diagonal is identical. At $T = 0$ for oscillators with $d = 3$, $\omega = 200$ cm^{-1}, temperature 298 K, and overdamped damping constant $\gamma = 440$ cm^{-1}, the cross width (the width perpendicular to the diagonal) of the critically damped oscillator spectrum is on the order of 1% greater than the overdamped spectrum. In the imaginary part, the nodal line in the critically

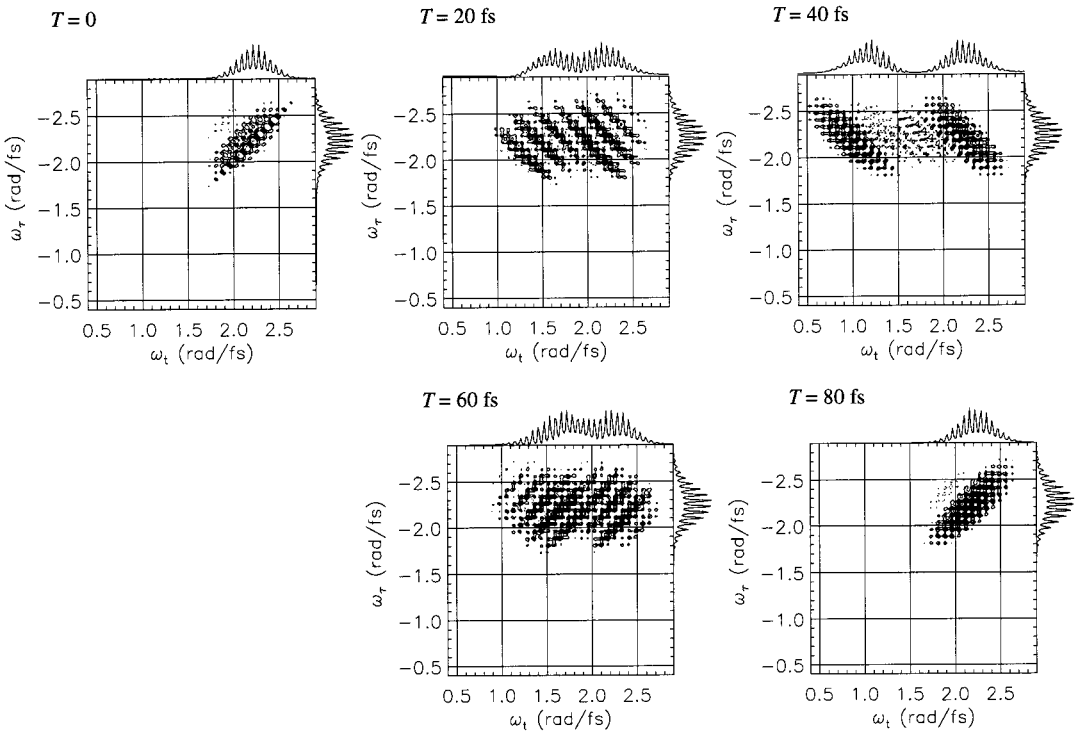

Figure 8. Real parts of the calculated impulsive 2D spectra for an underdamped Brownian oscillator at $T = 0$, 20, 40, 60, and 80 fs. The oscillator parameters are $\omega_{eg} = 10\,000$ cm^{-1}, $\lambda = 1800$ cm^{-1}, $d = 3$, $\omega = 400$ cm^{-1}, $\gamma = 10$ cm^{-1}, and temperature = 600 K. The projection of the 2D spectrum onto the ω_τ axis resembles the steady state absorption spectrum for all values of T. The projection onto the ω_t axis changes with T and equals the spectrally resolved pump−probe signal. The band structure in the spectrum changes as the wavepacket moves on the excited state surface. It is perpendicular to the diagonal as the wavepacket moves toward the low-frequency (outer) turning point and parallel to it when the wavepacket is moving back toward the high-frequency (inner) potential wall. This reflects the ability of 2D spectra to reveal phases, a consequence of detecting the complete electric field of the photon echo.

damped spectrum is approximately 5° more tilted away from vertical. As the damping of the overdamped oscillator gets larger, these differences will increase, but the shapes of the spectra will remain similar. Figure 9 shows the absorptive and dispersive parts of the spectrum for a critically damped Brownian oscillator and a Gaussian $M(t)$ at $T = 0$. Both 2D spectra in Figure 9 resemble a smeared out version of the underdamped 2D correlation spectrum in Figure 5b. At $T = 0$ all three solvation models give spectra with a slight asymmetry about the diagonal, i.e., decay more rapidly as a function of $(\omega_t - \omega_\tau)$ for $\omega_t < \omega_\tau$ than $\omega_t > \omega_\tau$.

A Gaussian $M(t)$ is most commonly used to model the inertial part of solvation, and as such we have investigated the 2D spectrum for this model in more detail. The projection-slice theorem[2,55,56] indicates the projection of the 2D spectrum perpendicular to the diagonal $\omega_\tau = -\omega_t$ is the Fourier transform of the signal field at times $t = \tau$.[76] This suggests that the 2D cross width $(\Delta\omega_c)$ perpendicular to the diagonal $\omega_t = -\omega_\tau$ represents photon echo decay and should be closely related to the frequency−frequency correlation function $M(t)$. Table 2 shows the inverse cross width of the 2D spectrum as a function of the time constant τ_g. The simulations were done with 128 t values and 128 τ values on a 200 fs × 256 fs grid, $\lambda = 1800$ cm^{-1}, $T = 0$, and a temperature of 298 K. For $\tau_g > 140$ fs, it is necessary to enlarge the time range of the calculation so that there will be sufficient frequency resolution to measure a width reliably. For $\tau_g < 90$ fs, the time step needs to be decreased to increase the frequency range of the calculation. This relationship between cross width and inertial Gaussian time constant may be useful for estimating the inertial solvation time constant for polar solvents.[68,77] Calculations on critically damped Brownian

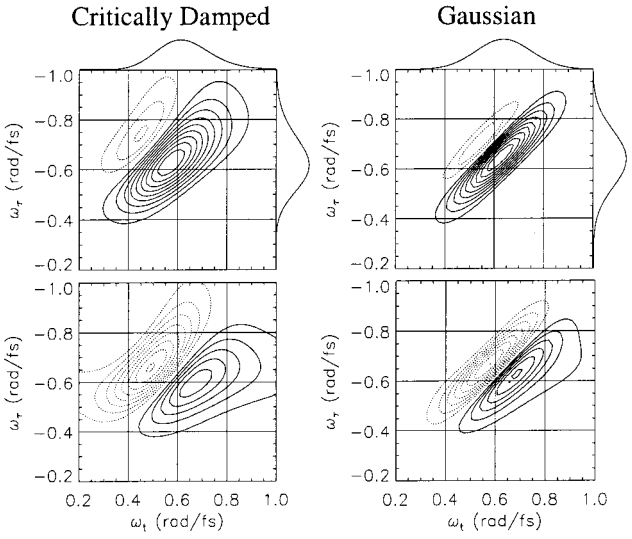

Figure 9. Impulsive 2D correlation spectra calculated with critically damped Brownian oscillator (left) and Gaussian (right) frequency correlation functions $M(t)$ used to model inertial solvation. Real parts of the 2D spectra are shown on top, imaginary below. Contour intervals are 10% of the real maximum. Dotted contours are negative. In both cases, $\omega_{eg} = 2500$ cm^{-1}, $\lambda = 900$ cm^{-1}, and $\Delta^2 = 2kT\lambda$ (where the temperature $T = 298$ K). The frequency of the critically damped oscillator is $\omega = 400$ cm^{-1}. The Gaussian time constant is $\tau_g = 100$ fs. The critically damped oscillator $M(t)$ has decayed to its half-maximum approximately 20 fs before the Gaussian $M(t)$, but both decay to ∼5% of their maximum value by 200 fs. The Gaussian spectrum is tilted more along the diagonal and has a smaller cross width perpendicular to the diagonal, but the projections of both spectra on the two frequency axes are almost identical.

TABLE 2: Gaussian Time Constant τ_g vs 2D Spectrum Inverse Cross Width

τ_g (fs)	$2\pi/\Delta\omega_c$ (fs)
90	67 ± 6
100	71 ± 3
110	74 ± 3
120	77 ± 3
130	80 ± 3
140	82 ± 3
150	86 ± 6

oscillators suggest the cross width is more closely related to decoherence[78] than dephasing.

Since the three-pulse echo peak shift is the simplest parameter recovered from prior photon echo studies,[31,32,34,35,71] it is important to understand how the peak shift is represented in 2D spectra. The three-pulse echo peak shift τ^* is the value of τ for which the three-pulse echo signal energy (integrated over t) is maximum. It is easily extracted from the time domain data used to calculate 2D spectra. Dephasing processes are quite conspicuous in the dispersive part of the 2D spectrum. The nodal line in the dispersive spectrum is tilted from the vertical when there is a "peak shift" in the integrated three-pulse echo signal. This tilted nodal line can occur for T greater than the pulse duration, when rephasing and nonrephasing contributions to the signal are equally weighted and indicates that the rephasing contribution to the signal is intrinsically stronger than the nonrephasing contribution. The three-pulse echo peak shift has been used to measure this difference in strength. This echo peak shift tilt in the 2D spectrum does not mix real and imaginary parts of the spectrum (see the discussion of the inhomogeneous Bloch model) and is distinctly different in origin from the "phase-twist" arising from unequally weighted rephasing vs nonrephasing signal contributions, where the real and imaginary parts of the spectrum are mixed. The echo tilt effect in 2D spectra depends on both the peak shift and the variation in photon echo emission time with τ. For a given value of T, multiplication of the spectrum by a frequency-dependent phase factor $\exp(i\omega_\tau\tau^*)$ will remove echo tilt caused by the peak shift.

To investigate solvation more closely, we calculated 2D spectra for a model solvent frequency correlation function $M(t) = A_g \exp(-t^2/\tau_g^2) + A_1 \exp(-t/\tau_1) + A_2 \exp(-t/\tau_2)$, where $A_g = 0.62$, $A_1 = 0.23$, $A_2 = 0.15$. $\tau_g = 105$ fs, $\tau_1 = 1400$ fs, and $\tau_2 = 11$ ps with total Stokes' shift, $2\lambda = 1208$ cm^{-1}. This is a common form[35,79−81] used to fit three pulse scattering signals with the intramolecular vibrational part of $M(t)$ removed to consider only the solvent. Figure 10a shows a spectrum calculated from such a "solvent $M(t)$" for impulsive pulses. 512 points were used in the FT with respect to the t axis, with 200 unevenly spaced Gaussian quadrature points interpolated onto the evenly spaced grid with cubic splines. In Figure 10a, the negative lobe appears only above the diagonal, and the spectrum has a narrower cross width than the Gaussian part alone. Even for slowly decaying exponentials, the decay of $M(t)$ near $t = 0$ will be faster than any Gaussian decay (due to the nonzero derivative of the exponential at $t = 0$) thus altering the 2D spectrum. For the first 10 fs the 1.4 ps exponential decay dominates $M(t)$. As a correlation function, $M(t)$ should have zero derivative at $t = 0$. From a physical point of view the Gaussian inertial solvation step produces the subsequent approximately exponential solvent relaxation, so both the complete decay of the Gaussian part of $M(t)$ and the exponential decays near zero are unphysical. Unlike the spectrum calculated from a purely Gaussian $M(t)$, it is not possible to simply read off the inertial solvation time from the cross width of the spectrum. The time constants of the exponentials and the relative contribution of each exponential to the Stokes' shift can be obtained from three-pulse echo peak shift measurements.[35,80,81] This means that by varying the Gaussian time constant τ_g and reorganization energy, the inertial solvation time can still be obtained by comparing calculated and measured 2D correlation spectra.

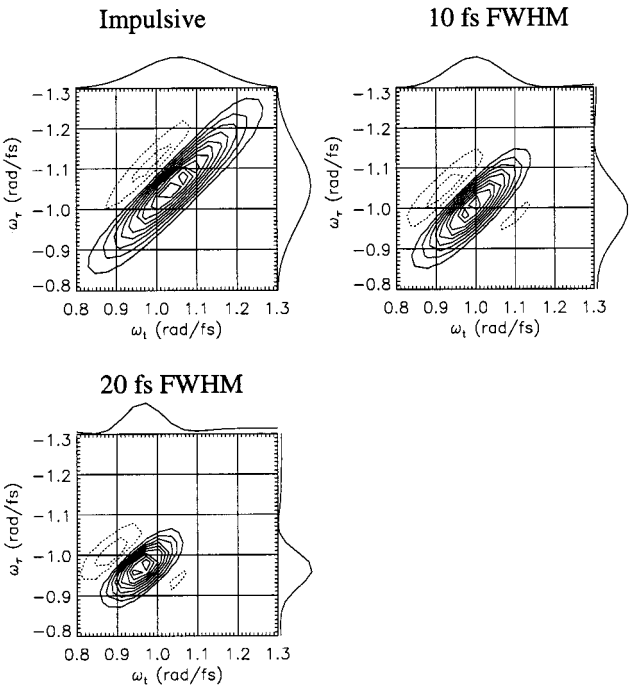

Figure 10. Room temperature (298 K) methanol solvent 2D correlation spectra (real part) $\omega_{eq} = 5000$ cm^{-1}. $\lambda = 604$ cm^{-1}, $M(t) = A_g \exp(-t^2/\tau_g^2) + A_1 \exp(-t/\tau_1) + A_2 \exp(-t/\tau_2)$, where $A_g = 0.62$, $A_1 = 0.23$, $A_2 = 0.15$. $\tau_g = 105$ fs, $\tau_1 = 1400$ fs, $\tau_2 = 11$ ps for three excitation pulse widths. (a, top left) impulsive; (b, top right) 10 fs; (c, bottom) 20 fs. While the extent of the spectrum along the diagonal varies dramatically, the cross width perpendicular to the diagonal is almost unchanged. The excitation pulse spectrum essentially acts as a filter for both dimensions of the 2D spectrum. This lack of distortion makes it possible to characterize events that cannot be measured with standard time domain techniques.

Since all the calculations described so far to demonstrate the solvation information contained in the 2D spectrum have used impulsive 0.1 fs pulses, it is natural to ask whether the same information can still be obtained using experimentally realizable pulse lengths. Hybl et al. conjectured that a finite pulse duration essentially filters 2D spectra by the pulse spectrum in the frequency domain. Calculations for Brownian oscillators confirm this suggestion. More stringent tests are described below. Calculated 2D correlation spectra for the solvent $M(t)$ given above using 10 and 20 fs intensity fwhm transform-limited pulses are shown in Figure 10, b and c, respectively. The effect of pulse duration on the 2D cross width is remarkably small. As the pulse width increases (and the bandwidth decreases) the extent of the spectra along the diagonal decreased by a factor of ~2.5 from impulsive to 20 fs fwhm, but the cross width decreased only by ~5% from impulsive to 20 fs. When the pulse length goes from impulsive to 20 fs, there is a 0.003 ± 0.001 rad/fs (1.5 cm^{-1}) measured decrease in the peak cross width. This corresponds to a pulse width distortion induced 5 fs increase in the Gaussian inertial solvation time read off the 2D spectrum. This slight distortion can be readily accounted for by fitting the data with the known pulse duration. As long as the excitation pulses have enough bandwidth to cover the cross width of the spectrum, it is possible to get an accurate estimate of the inertial solvation time from a 2D spectrum.

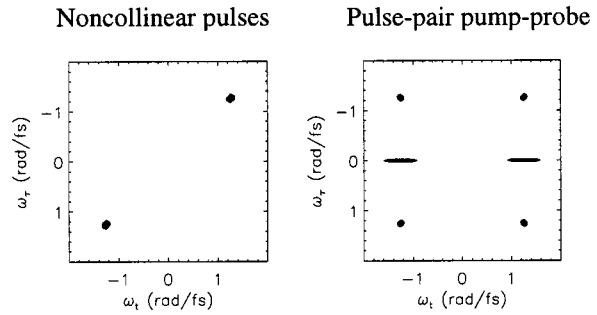

Figure 11. Comparison between the real 2D FT spectrum calculated for three noncollinear pulses and a 2D spectrum calculated for a spectrally resolved pulse-pair pump−probe signal with a collinear pump pulse-pair and a noncollinear probe. The time domain pulse-pair pump−probe signal showed 10% modulation around $\tau = 0$. Both spectra were calculated for 10 fs fwhm excitation pulses at $T = 0$ using a Bloch model ($g(t) = \Gamma t$) with $\Gamma = 300$ cm^{-1}, and $\omega_{eg} = 6000$ cm^{-1}. The noncollinear spectrum shows two peaks, one at $(\omega_\tau, \omega_t) = (-\omega_{eg}, \omega_{eg})$ and one at $(\omega_{eg}, -\omega_{eg})$ while the collinear 2D spectrum has signal peaks in all four quadrants as well as peaks from the third excitation pulse and single-pulse pump−probe signals at $(0, \omega_{eg})$ and $(0, -\omega_{eg})$.

IVC. Absorption Mode 2D. The experimental apparatus for EASY 2D spectroscopy is complex, and a simpler implementation which produces pure absorption mode 2D spectra seems desirable for some applications. In magnetic resonance, experiments which produce amplitude-modulated signals yield pure absorption mode 2D spectra. The technique proposed here consists of collinear pulse pair excitation followed by measurement of the spectrum of a third, noncollinear probe pulse.[82] This method sorts the spectrally resolved pump−probe signal according to the excitation frequency by Fourier transformation with respect to the collinear pulse pair delay, which amplitude-modulates the signal. Since the probe spectrum is real, a symmetrical scan of the pulse pair will produce a real 2D spectrum upon Fourier transformation. Since the probe acts as both excitation source for the nonlinear signal and a temporally overlapping (homotime)[38] reference field for interference detection, this is homotime absorptive response detection, or HARD 2D spectroscopy. The question arises whether the purely real HARD 2D spectrum is identical to the real part of the EASY 2D spectrum. This question was first investigated computationally by Gallagher Faeder.[68] Computational and analytical results will be presented here.

Calculations of the pulse-pair pump−probe third-order polarization must include response functions for both the $\boldsymbol{k}_{sa} = -\boldsymbol{k}_a + \boldsymbol{k}_b + \boldsymbol{k}_c$ and $\boldsymbol{k}_{sb} = \boldsymbol{k}_a - \boldsymbol{k}_b + \boldsymbol{k}_c$ phase matching directions (since $\boldsymbol{k}_{sa} = \boldsymbol{k}_{sb} = \boldsymbol{k}_c$). As in the three-pulse echo, pulses *a* and *b* are scanned so that T remains constant. The sum of the excitation and signal fields with wave vector $\boldsymbol{k}_c$ is transformed with respect to t and the resulting spectrum $I(\omega_t,\tau,T)$ is transformed with respect to τ. One consequence of the interchangeability of collinear pulses *a* and *b* is that the real signal spectrum is symmetric around zero with respect to τ. At each ω_t, the ω_τ spectrum calculated from a signal that is real and even is itself real and even,[66] so the 2D FT spectrum has all its amplitude in the real part. In Figure 11 a calculated HARD 2D FT spectrum is compared to the real part of an EASY 2D FT spectrum. Each spectrum was calculated at $T = 0$ using the Bloch model [$g(t) = \Gamma t$], with $\omega_{eg} = 6000$ cm^{-1}, $\Gamma = 300$ cm^{-1}, and 10 fs intensity fwhm pulses. The noncollinear EASY 2D spectrum shows two signal peaks, one at $(\omega_t, \omega_\tau) = (\omega_{eg}, -\omega_{eg})$ and the other at $(-\omega_{eg}, \omega_{eg})$. The pulse-pair pump−probe time domain signals were modulated by 10% around $\tau = t_b - t_a = 0$, when pulses a and b were overlapped. The pulse-pair pump−probe HARD 2D spectrum shows signal peaks in all four quadrants [at $(\omega_t, \omega_\tau) = (\omega_{eg}, \omega_{eg})$, $(\omega_{eg}, -\omega_{eg})$, $(-\omega_{eg}, -\omega_{eg})$, and $(-\omega_{eg}, \omega_{eg})$] as well as peaks from the third excitation pulse and the pump−probe contributions at $(\pm\omega_{eg}, 0)$.

Close examination of the region $\omega_t = -\omega_\tau = 0.7$ to 1.2 rad/fs revealed peak shapes that were identical to within the noise of the calculation and both matched the partially phase-twisted peakshape in Figure 4.[68] The pulse-pair pump−probe 2D FT spectrum has the same information as the real part of the noncollinear 2D FT spectrum. Since the Bloch model has no Stokes' shift, 2D FT spectra were calculated for a Brownian oscillator with a Gaussian $M(t)$ also. 2D spectra calculated at $T = 0$ for $M(t) = \exp(-t^2/\tau_g^2)$, with $\lambda = 900$ cm^{-1}, $\tau_g = 100$ fs, temperature = 298 K, and impulsive pulses showed excellent agreement between the HARD 2D and real EASY 2D peak shapes.[68] Since EASY 2D spectra have dispersion in ω_t, and HARD 2D spectra do not, this is an example where 2D *power* spectra have different peak shapes because of the phase-matching and scan procedure.

The computational results suggest HARD 2D measures the real part of the EASY 2D spectrum and this similarity is now explored analytically. The nonlinear polarization in a HARD 2D experiment is given by

$$P^{(3)}_{\mathrm{HARD}}(t,t_a,t_b) = P^{(3)}(\boldsymbol{k}_{sa},t,t_a,t_b) + P^{(3)}(\boldsymbol{k}_{sb},t,t_a,t_b) \quad (19)$$

Using the result $S^{(3)}(\boldsymbol{k}_{sb},\tau_b,\tau_a,\tau_c) = S^{(3)}(\boldsymbol{k}_{sa},\tau_a,\tau_b,\tau_c)$ obtained by symmetry between the two phase-matching directions, the HARD 2D nonlinear polarization is

$$P^{(3)}_{\mathrm{HARD}}(t,t_a,t_b) = P^{(3)}(\boldsymbol{k}_{sa},t,t_a,t_b) + P^{(3)}(\boldsymbol{k}_{sa},t,t_b,t_a) \quad (20)$$

which is the unique even extension of the unsymmetrical EASY 2D nonlinear polarization with respect to $\tau = t_b - t_a$. This provides the unique even and hence real extension of the spectrum in the ω_τ dimension. The spectrum detected in a HARD 2D experiment can be written as

$$I(\omega_t,t_a,t_b) \propto |\hat{E}_c(\omega_t) + i\omega_t[\hat{P}^{(1)}_c(\omega_t) + \hat{P}^{(3)}_{\mathrm{HARD}}(\omega_t,t_a,t_b) + \hat{P}^{(3)}_{\mathrm{ppa}}(\omega_t,t_a,t_a) + \hat{P}^{(3)}_{\mathrm{ppb}}(\omega_t,t_b,t_b)]|^2 \quad (21)$$

where the radiated field consists of a linear free induction decay from pulse c, the desired HARD 2D field, and single-pulse pump−probe signal fields from pulses a and b. The HARD 2D signal can be isolated by a number of subtraction schemes (e.g. phase cycling, lock-in detection) or simply separated by Fourier transformation with respect to τ. The HARD 2D signal consists only of the cross terms between the HARD 2D field and pulse *c* (including free induction decay) and is clearly real.

$$\Delta I_{\mathrm{HARD}}(\omega_t,t_a,t_b) \propto i\omega_t\hat{P}^{(3)}_{\mathrm{HARD}}(\omega_t,t_a,t_b)\,\hat{E}_c(\omega_t)^* - i\omega_t\hat{P}^{(3)}_{\mathrm{HARD}}(\omega_t,t_a,t_b)^*\,\hat{E}_c(\omega_t) \quad (22)$$

Using eq 4, eq 22 can be rearranged as

$$\Delta I_{\mathrm{HARD}}(\omega_t,t_a,t_b) \propto i\omega_t\hat{P}^{(3)}_{\mathrm{HARD}}(\omega_t,t_a,t_b)\,\hat{E}_c(\omega_t)^* + i(-\omega_t)\,\hat{P}^{(3)}_{\mathrm{HARD}}(-\omega_t,t_a,t_b)\,\hat{E}_c(-\omega_t)^* \quad (23)$$

which is an even function of frequency ω_t and thus the unique even extension of $i\omega_t\hat{P}^{(3)}_{\mathrm{HARD}}(\omega_t,t_a,t_b)\,\hat{E}_c(\omega_t)^*$ with respect to the signal frequency ω_t. This differs from the EASY 2D spectrum only because it is multiplied by $\hat{E}_c(\omega_t)^*$, but it should be kept in mind that the signal field in the detected EASY 2D spectral

interferograms are multiplied by the reference field envelope in a similar manner. For sufficiently broad pulse spectra, the reference field can be divided out in either case. We conclude that the HARD 2D spectrum is essentially equivalent to the real part of an EASY 2D spectrum. In particular, the amplitude-modulated HARD 2D spectrum has the same partial phase twist as the EASY 2D spectrum when "improperly time ordered" diagrams contribute to the signal. The partial phase twist for $T < t_p$ in real HARD 2D spectra arises because the probe is noncollinear with the pump pulse pair. In a two-level system, when all three pulses are collinear, inclusion of diagrams for $\boldsymbol{k}_{sa}$, $\boldsymbol{k}_{sb}$, and $\boldsymbol{k}_{sc} = \boldsymbol{k}_a + \boldsymbol{k}_b - \boldsymbol{k}_c$ yields a three-pulse signal with N/P balance for all T.

Since the center of pulse c defines $t = 0$, transform-limited pulses (real frequency domain field $\hat{E}_c(\omega_t)$) selectively detect the real part of the HARD signal field. For transform-limited pulses without phase shifts, eqs 5 and 22 can be used to show that the full HARD 3D spectrum generated by complex Fourier transformation with respect to t, t_a, and t_b is sensitive only to the imaginary (dissipative) part of $\hat{S}^{(3)}(\boldsymbol{k}_{sa}, -\omega_a,\omega_b,\omega_c)$. A similar result has been obtained for the heterodyne-detected stimulated photon echo (HSPE) by Albrecht et al.[38] We suspect 2D spectra recorded using the HSPE would be equivalent to HARD 2D.

V. Discussion

Separating the absorptive and dispersive parts of 2D Fourier transform spectra has a number of advantages: it provides simple relationships between 2D spectra and other nonlinear experiments, increases resolution and information content, and reveals homogeneous line shapes masked by inhomogeneous broadening. A full separation requires the experiment to equally weight N and P type coherence pathways in the signal and careful choice of Fourier transformations to match the data. The procedure developed by Hybl et al.[1] is remarkably successful in this regard, but does produce partially mixed peak shapes when T is less than the pulse duration or four different levels are simultaneously involved in producing a four-wave mixing signal.

The real part of the 2D spectrum can be viewed as a Fourier separation of the spectrally resolved pump−probe signal according to initial dipole oscillation frequency. Although the spectrally resolved pump−probe signal is the change in transmitted probe spectrum caused by the pump, this change includes coherent Raman scattering (not just stimulated emission from the excited state and reduction of ground state absorption by population depletion).[21] This generalized absorption difference spectrum preserves useful interference effects. The wavepacket dynamics in Figure 8 vividly illustrate these interference effects—entire regions of the 2D spectrum appear and disappear as the vibrational wavepackets oscillate coherently back and forth. The vibrational dynamics in the 2D spectrum reveal phase relations between the various transition dipole matrix elements that cannot yet be directly measured by optical frequency domain techniques. The generalized absorption correlation in 2D FT spectra provides new information compared to rigorously absorptive 2D correlation spectra, which reveal only squares of matrix elements. It is a virtue of 2D FT techniques to preserve as much of this phase information as possible.

After sublevel coherence has decayed away, twisted peak shapes do not appear in the 2D electronic relaxation spectra and there is a good correspondence between 2D electronic relaxation spectroscopy and 2D NMR relaxation spectra (NOESY) at the vibronic level. Peaks in both 2D relaxation spectra have real absorption and imaginary dispersion line shapes. Rigorously, the real part of the 2D spectrum represents absorption coefficient frequency correlation while the imaginary part displays correlation between initial absorption frequency and subsequent frequency-dependent refractive index changes. A simple absorption−emission correlation picture, when generalized to moving wavepackets, explains most of the intensity in all of the 2D spectra calculated here.

The correspondence between 2D electronic correlation spectra and 2D NMR correlation spectra (COSY) is clouded by twisted peak shapes arising from rephasing/nonrephasing imbalance in the electronic correlation spectra and the pulse area dependent peakshapes in COSY NMR spectra. Four-level signals contribute to 2D NMR correlation spectra when there is strong spin−spin coupling,[2,64,65] and strongly coupled spin systems yield mixed COSY peak shapes.[2,3] 2D electronic correlation spectra have qualitative similarities to strongly coupled spin systems in COSY 2D NMR, but investigations using models with well-resolved, nonoverlapping transitions seem desirable.

The information content of 2D spectra is dramatically improved by separation into real and imaginary parts even when partially twisted peakshapes are obtained, as in the $T = 0$ correlation experiments. When mixed peak shapes appear, the complex 2D spectrum displays correlation of both amplitude and phase between initial and final dipole oscillation frequencies. The connection between absorption/dispersion and real/imaginary parts of these mixed 2D signals needs to be addressed. HARD 2D, an experiment which is sensitive only to the imaginary (dissipative) part of the fully noncollinear phase-matched third-order susceptibility $\hat{S}^{(3)}(\boldsymbol{k}_{sa}, -\omega_a,\omega_b,\omega_c)$, produces a partly phase-twisted peakshape at $T = 0$ for a two-level Bloch model when cosine transforms are applied to real cosinusoidal data. The mixed peak shape in the real HARD 2D correlation spectrum originates from noncollinear phase matching and therefore reflects bulk phase matching in $\hat{S}^{(3)}$, not a molecular response.

2D Fourier transform spectroscopy provides an extremely simple and powerful way to visualize nonlinear experiments as absorption correlation, but 2D FT methods are not just a visualization technique. The power of 2D FT techniques over conventional nonlinear techniques such as pump−probe or photon echoes comes from the exploitation of coherence and phase information to generate a new frequency axis (which may be of a completely new type). A distinguishing feature of 2D FT methods treated here is that the frequency resolution in each dimension is limited only by how long a single dipole oscillates coherently with itself. 2D sorting of final frequencies by initial frequencies reveals this correlation, which is usually hidden under the inhomogeneous line shape. 2D FT spectroscopy is in many ways complementary to single molecule techniques:[83−85] single-molecule spectroscopy requires a time average over repeated optical excitations while 2D spectra require a single weakly nonlinear excitation which is sorted by frequency to recover an ensemble of single molecule correlations directly on the timescale of molecular motion.

2D FT methods are wonderfully immune to pulse duration effects. A longer pulse appears to simply limit the range of a 2D spectrum by acting as a frequency domain filter. The shortest available pulses are desirable because a broad spectrum does not limit frequency resolution in 2D FT spectroscopy. As in 1D FT spectroscopy,[57] the frequency resolution of 2D FT spectra is limited only by the maximum separation between pulses used to generate the measured signal, not by the pulse bandwidth. 2D FT methods completely solve the problem of trading frequency resolution for time resolution encountered in femto-

second spectroscopy.[73] This means that it may be possible to use a "universal" broadband 2D FT spectrometer based on the shortest pulses available for any nonlinear experiment covered by the pulse spectrum.

The model methanol 2D spectra calculated here are in qualitative agreement with the previously reported 2D electronic correlation spectrum for IR144 in methanol (Figure 3 of Hybl et al.).[1] The negative region above the diagonal in the calculations shown here in Figure 9 was not previously observed experimentally, but lies just below the lowest reported contour in Figure 3 of Hybl et al.[1] This negative region persists when IR 144 intramolecular vibrations are included in the model. Since the prediction of the negative region above the diagonal, experimental improvements have allowed its unambiguous observation.[68,77] The ability of 2D spectroscopy to recover an almost undistorted Gaussian inertial response by examination of the cross-width is very promising for studies of femtosecond solvent reorganization. A more detailed investigation of the early time solvent dynamics is underway.

The techniques HARD 2D and EASY 2D have a close relationship with contrasting experimental requirements. HARD 2D requires only three beams and relatively low spectrometer resolution, but does not allow adjustment of the local oscillator strength for optimized interference detection. HARD 2D also requires either phase cycling or Nyquist sampling at the highest frequency in the signal. Warren and co-workers have discussed advantages of phase cycling in partially collinear two-dimensional optical experiments.[86] Drawbacks of EASY 2D include the required five beams and passive interferometric stability. Advantages of EASY 2D include full separation of coherence orders for temporally nonoverlapping beams, optimized interference detection, and ability to systematically undersample without phase cycling.

It is an interesting question whether tunable pump/broadband probe experiments[12] can be used to reconstruct[55] the broadband 2D FT spectrum. Terms in the four-wave mixing signal involving four different frequencies (e.g. subdiagrams d_7 and d_8 in Figure 3) suggest not. In the absence of a robust reconstruction technique, the resolution in the pump frequency dimension of the tunable pump/broadband probe methods is limited by both the pump spectrum and sample relaxation during the pump pulse. This differs from the molecule limited frequency resolution in both dimensions of broadband 2D FT spectra and confers a practical advantage to 2D FT spectra.

VI. Conclusions

Analysis of two-dimensional Fourier transform correlation and relaxation experiments for two electronic states each having two or more sublevels shows that the separation into real and imaginary parts has powerful advantages. The NMR concept of coherence order was extended to nonlinear optics to transpose real/imaginary separation techniques of 2D NMR to 2D optical spectroscopy. The phase-matching geometry, scan procedure, and method of Fourier transforming the data have a strong influence on the real/imaginary separation and even the shape of the absolute value 2D spectrum. An experimental method for obtaining only the real part of the 2D spectrum was proposed. Under favorable circumstances, the 2D real/imaginary separation can be understood as a separation of nonlinear absorption coefficient changes (real part of 2D spectrum) from nonlinear refractive index changes (imaginary part of 2D spectrum). Phase-twisted peaks, which mix absorption and dispersion line shapes, can occur when pulses overlap or coherent sublevel superposition states are excited. An increase in transform-limited excitation pulse duration is found to limit the range of a 2D spectrum by spectral filtering without significantly distorting the underlying structure. The projection of the complex 2D spectrum onto the detection frequency ω_t equals the transient grating signal field and the real part of this projection gives the spectrally resolved pump−probe signal. Reciprocally, 2D electronic spectra can be understood as separating these 1D signals according to initial dipole oscillation frequency. Calculated 2D spectra for an underdamped Brownian oscillator reveal a band structure within the wavepacket that is not apparent in the spectrally resolved pump−probe signal. Assignment of 2D spectra with vibronic structure was discussed, and the signatures of vibrational relaxation in 2D spectra were explored. Calculated 2D spectra for models of polar solvent dynamics showed that the diagonal cross-width of the real 2D spectrum tracks the frequency−frequency correlation function $M(t)$. These 2D spectra can be qualitatively understood as separating the absorption spectra of molecules in different solvent environments by correlating absorption and emission on a timescale faster than solvent rearrangement. The calculations presented here exhibit a wealth of information in the separate real and imaginary peakshapes of 2D Fourier transform electronic spectra. The high time resolution, single weakly nonlinear excitation, and ability of 2D separation to reveal the distribution and correlation of spectral properties in an ensemble suggest 2D FT spectroscopy may be a powerful complement to single molecule techniques.

Acknowledgment. We thank John Hybl for many useful and stimulating conversations and Kurt Zilm for pointing out that imbalanced N and P coherence could lead to distortions in 2D spectra. Warren generously provided a preprint of a related manuscript (ref 86) prior to publication. This work was supported by the Camille and Henry Dreyfus Foundation, the David and Lucile Packard Foundation, and the National Science Foundation. D.M.J. is an Alfred P. Sloan Research Fellow. This paper is dedicated to Kent Wilson in gratitude for his enthusiastic support and early encouragement of our work.

References and Notes

(1) Hybl, J. D.; Albrecht, A. W.; Gallagher Faeder, S. M.; Jonas, D. M. *Chem. Phys. Lett.* **1998**, *297*, 307−313.

(2) Ernst, R. R.; Bodenhausen, G.; Wokaun, A. *Principles of Nuclear Magnetic Resonance in One and Two Dimensions*; Oxford Press: London, 1987.

(3) Cavanaugh, J.; Fairbrother, W. J.; Palmer, III, A. G.; Skelton, N. J. *Protein NMR Spectroscopy: principles and practice*; Academic Press: San Diego, CA, 1996.

(4) Tanimura, Y.; Mukamel, S. *J. Chem. Phys*. **1993**, *99*, 9496−9511.

(5) Tokmakoff, A.; Lang, M. J.; Larsen, D. S.; Fleming, G. R.; Chernyak, V.; Mukamel, S. *Phys. Rev. Lett*. **1997**, *79*, 2702−2705.

(6) Okumura, K.; Tanimura, Y. *Chem. Phys. Lett*. **1998**, *295*, 298−304.

(7) Chernyak, V.; Zhang, W. M.; Mukamel, S. *J. Chem. Phys*. **1998**, *109*, 9587.

(8) Park, K.; Cho, M. *J. Chem. Phys.* **1998**, *109*, 10559−10569.

(9) Mukamel, S.; Piryatinski, A.; Chernyak, V. *Acc. Chem. Res*. **1999**, *32*, 145−154.

(10) Zhang, W. M.; Chernyak, V.; Mukamel, S. *J. Chem. Phys*. **1999**, *110*, 5011−5028.

(11) Deak, J. C.; Iwaki, L. K.; Dlott, D. D. *J. Phys. Chem. A* **1998**, *102*, 8193−8201.

(12) Hamm, P.; Lim, M.; DeGrado, W. F.; Hochstrasser, R. M. *Proc. Natl. Acad. Sci. U.S.A.* **1999**, *96*, 2036−2041.

(13) Cong, P.; Yan, Y. J.; Deuel, H. P.; Simon, J. D. *J. Chem. Phys*. **1994**, *100*, 7855−7866.

(14) Rossky, P. J.; Simon, J. D. *Nature* **1994**, *370*, 263−269.

(15) Jimenez, R.; Fleming, G. R.; Kumar, P. V.; Maroncelli, M. *Nature* **1994**, *369*, 471−473.

(16) Laenen, R.; Rauscher, C.; Laubereau, A. *Phys. Rev. Lett*. **1998**, *80*, 2622−2625.

(17) Jonas, D. M.; Lang, M. J.; Nagasawa, Y.; Joo, T.; Fleming, G. R. *J. Phys. Chem*. **1996**, *100*, 12660−12673.
(18) Lin, S.; Taguchi, A. K. W.; Woodbury, N. W. *J. Phys. Chem*. **1996**, *100*, 17067−17078.
(19) Brito Cruz, C. H.; Gordon, J. P.; Becker, P. C.; Fork, R. L.; Shank, C. V. *IEEE J. Quantum Elect*. **1988**, *24*, 261−265.
(20) Fragnito, H. L.; Bigot, J.-Y.; Becker, P. C.; Shank, C. V. *Chem. Phys. Lett*. **1989**, *160*, 101−104.
(21) Pollard, W. T.; Dexheimer, S. L.; Wang, Q.; Peteanu, L. A.; Shank, C. V.; Mathies, R. A. *J. Phys. Chem*. **1992**, *96*, 6147−6158.
(22) Arnett, D. C.; Moser, C. C.; Dutton, P. L.; Scherer, N. F. *J. Phys. Chem. B* **1999**, *103*, 2014−2032.
(23) Aue, W. P.; Bartholdi, E.; Ernst, R. R. *J. Chem. Phys*. **1976**, *64*, 2229−2246.
(24) Vogelsanger, B.; Bauder, A. *J. Chem. Phys*. **1990**, *92*, 4101−4114.
(25) Vogelsanger, B.; Andrist, M.; Bauder, A. *Chem. Phys. Lett*. **1998**, *144*, 180−186.
(26) Suter, D.; Klepel, H.; Mlynek, J. *Phys. Rev. Lett*. **1991**, *67*, 2001−2004.
(27) Suter, D.; Klepel, H. *Europhys. Lett*. **1992**, *19*, 469−474.
(28) Lepetit, L.; Joffre, M. *Opt. Lett*. **1996**, *21*, 564−566.
(29) Blank, D. A.; Kaufman, L. J.; Fleming, G. R. *J. Chem. Phys*. **1999**, *111*, 3105−3114.
(30) Ulness, D. J.; Kirkwood, J. C.; Albrecht, A. C. *J. Chem. Phys*. **1998**, *108*, 3897−3902.
(31) de Boeij, W. P.; Pshenichnikov, M. S.; Wiersma, D. A. *Chem. Phys. Lett*. **1996**, *253*, 53−60.
(32) Cho, M.; Yu, J.-Y.; Joo, T.; Nagasawa, Y.; Passino, S. A.; Fleming, G. R. *J. Phys. Chem*. **1996**, *100*, 11944−11953.
(33) Gallagher, S. M.; Albrecht, A. W.; Hybl, J. D.; Landin, B. L.; Rajaram, B.; Jonas, D. M. *J. Opt. Soc. Am. B* **1998**, *15*, 2338−2345.
(34) Weiner, A. M.; Desilvestri, S.; Ippen, E. P. *J. Opt. Soc. Am. B* **1985**, *2*, 654−661.
(35) Joo, T.; Jia, Y.; Yu, J.-Y.; Lang, M. J.; Fleming, G. R. *J. Chem. Phys*. **1996**, *104*, 6089−6108.
(36) Mukamel, S. *Principles of Nonlinear Optical Spectroscopy*; Oxford University Press: New York, 1995.
(37) Nelson, K. A.; Casalegno, R.; Miller, R. J. D.; Fayer, M. D. *J. Chem. Phys*. **1982**, *77*, 1144−1152.
(38) Albrecht, A.; Hybl, J. D.; Gallagher Faeder, S. M.; Jonas, D. M. *J. Chem. Phys*., in press.
(39) Warren, W. S.; Zewail, A. H. *J. Chem. Phys*. **1983**, *78*, 2279−2297.
(40) Kawashima, H.; Wefers, M. M.; Nelson, K. A. *Annu. Rev. Phys. Chem*. **1995**, *46*, 627−656.
(41) Tull, J. X.; Dugan, M. A.; Warren, W. S. *Adv. Magn. Opt. Reson*. **1997**, *20*, 1−66.
(42) Williams, S.; Rahn, L. A.; Zare, R. N. *J. Chem. Phys*. **1996**, *104*, 3947−3955.
(43) Gallagher Faeder, S. M.; Jonas, D., manuscript in preparation.
(44) Landau, L. D.; Lifschitz, E. M.; Pitaevskii, L. P. *Electrodynamics of Continuous Media*, 2nd ed.; Pergamon Press: New York, 1984.
(45) Shen, Y. R. *The Principles of Nonlinear Optics*; Wiley-Interscience: New York, 1984.
(46) Yariv, A. *Quantum Electronics*, 2nd ed.; John Wiley and Sons: New York, 1975.
(47) Abella, I. D.; Kurnit, N. A.; Hartmann, S. R. *Phys. Rev*. **1966**, *141*, 391−406.
(48) Mukamel, S. *Annu. Rev. Phys. Chem*. **1990**, *41*, 647−681.
(49) Yan, Y. J.; Mukamel, S. *J. Chem. Phys*. **1988**, *89*, 5160−5176.
(50) Tanimura, Y.; Mukamel, S. *Phys. Rev. E* **1993**, *47*, 118−136.
(51) Gu, Y.; Widom, A.; Champion, P. M. *J. Chem. Phys*. **1994**, *100*, 2547−2560.
(52) Bardeen, C. J.; Shank, C. V. *Chem. Phys. Lett*. **1994**, *226*, 310−316.
(53) de Boeij, W. P.; Pshenichnikov, M. S.; Duppen, K.; Wiersma, D. A. *Chem. Phys. Lett*. **1994**, *224*, 243−252.
(54) Brabec, T.; Krausz, F. *Phys. Rev. Lett*. **1997**, *78*, 3282−3285.
(55) Mersereau, R. M.; Oppenheim, A. V. *Proc. IEEE* **1974**, *62*, 1319−1338.
(56) Nagayama, K.; Bachmann, P.; Wüthrich, K.; Ernst, R. R. *J. Magn. Reson*. **1978**, *31*, 133−148.
(57) Marshall, A. G.; Verdun, F. R. *Fourier Transforms in NMR, Optical, and Mass Spectrometry: a User's Handbook*; Elsevier Science Publishing: New York, 1990.
(58) Weitekamp, D. P. *Adv. Magn. Reson*. **1983**, *11*, 111−274.
(59) Bloembergen, N. *Nonlinear Optics*; Addison-Wesley: New York, 1992.
(60) Pechukas, P. *Phys. Rev. Lett*. **1994**, *73*, 1060−1062.
(61) Duppen, K.; Wiersma, D. A. *J. Opt. Soc. Am. B* **1986**, *3*, 614−621.
(62) Lee, D.; Albrecht, A. C. *Adv. Chem. Phys*. **1993**, *83*, 43−87.
(63) Demtröder, W. *Laser Spectroscopy*, 2nd ed.; Springer-Verlag: New York, 1982.
(64) Bodenhausen, G.; Freeman, R.; Morris, G. A.; Turner, D. L. *J. Magn. Reson*. **1977**, *28*, 17−28.
(65) Bodenhausen, G.; Freeman, R.; Morris, G. A.; Turner, D. L. *J. Magn. Reson*. **1978**, *31*, 75−95.
(66) Press, W. H.; Teukolsky, S. A.; Vetterling, W. T.; Flannery, B. P. *Numerical Recipes in C*, 2nd ed.; Cambridge University Press: Cambridge, UK, 1992.
(67) Numerical Recipes Software. *Numerical Recipes in Fortran*; Numerical Recipes Software: Cambridge, MA, 1996.
(68) Gallagher Faeder, S. M. Ph.D. Thesis, University of Colorado, 1999.
(69) Yang, T.-S.; Vohringer, P.; Arnett, D. C.; Scherer, N. F. *J. Chem. Phys*. **1995**, *103*, 8346−8359.
(70) Carter, E. A.; Hynes, J. T. *J. Chem. Phys*. **1991**, *94*, 5961−5979.
(71) de Boeij, W. P.; Pshenichnikov, M. S.; Wiersma, D. A. *J. Phys. Chem*. **1996**, *100*, 11806−11823.
(72) Lee, S.-H.; Lee, J.-H.; Joo, T. *J. Chem. Phys*. **1999**, *110*, 10969−10977.
(73) Jonas, D. M.; Bradforth, S. E.; Passino, S. A.; Fleming, G. R. *J. Phys. Chem*. **1995**, *99*, 2594−2608.
(74) Cina, J. A.; Smith, T. J. *J. Chem. Phys*. **1993**, *98*, 9211−9214.
(75) The nonlinear response functions used for these calculations are not in their high-temperature region of validity at 200 K.
(76) Note that the theorem says a complex projection *over all four quadrants* of the 2D spectrum equals an inverse Fourier transform of a real electric field.
(77) Hybl, J. D.; Albrecht, A. W.; Gallagher Faeder, S. M.; Jonas, D. M., manuscript in preparation.
(78) Prezhdo, O. V.; Rossky, P. J. *Phys. Rev. Lett*. **1998**, *81*, 5294−5297.
(79) Passino, S. A.; Nagasawa, Y.; Joo, T.; Fleming, G. *J. Phys. Chem*. **1996**, *101*, 725−731.
(80) Passino, S. A.; Nagasawa, Y.; Fleming, G. R. *J. Chem. Phys*. **1997**, *107*, 6094−6108.
(81) Nagasawa, Y.; Yu, J.-Y.; Fleming, G. R. *J. Chem. Phys*. **1998**, *109*, 6175−6183.
(82) Emde, M. F.; de Boeij, W. P.; Pshenichnikov, M. S.; Wiersma, D. A. *Opt. Lett*. **1997**, *22*, 1338−1340.
(83) Moerner, W. F.; Kador, L. *Phys. Rev. Lett*. **1989**, *62*, 2535−2538.
(84) Trautman, J. K.; Macklin, J. J.; Brus, L. E.; Betzig, E. *Nature* **1994**, *369*, 40−42.
(85) Lu, H. P.; Xie, X. S. *Nature* **1997**, *385*, 143−146.
(86) Keusters, D.; Tan, H.-S.; Warren, W. S. *J. Phys. Chem. A*, submitted for publication.